Article

Control of gasdermin D oligomerization and pyroptosis by the Ragulator-Rag-mTORC1 pathway

Graphical abstract
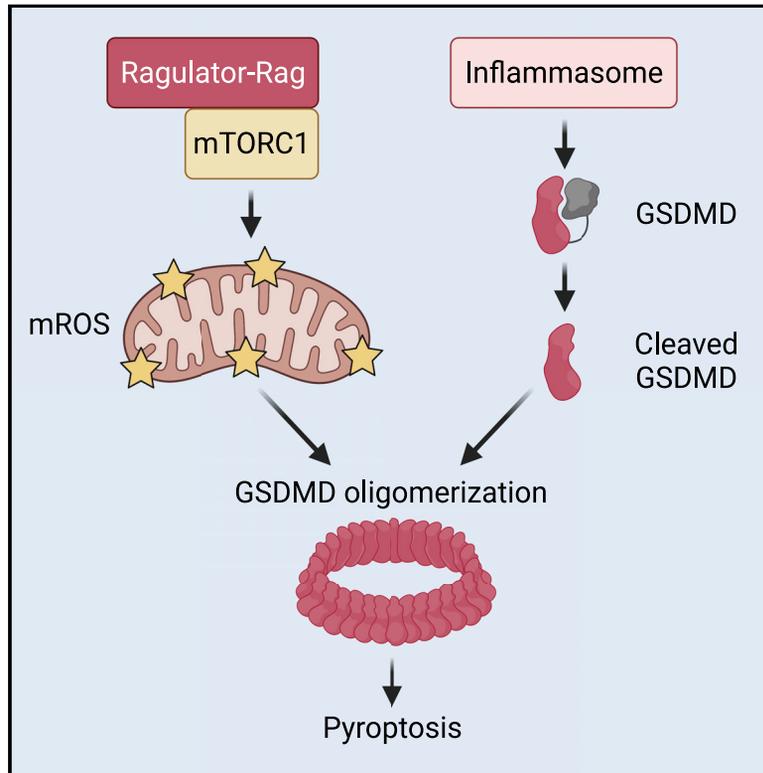
Authors

Charles L. Evavold, Iva Hafner-Bratkovič, Pascal Devant, ..., Arlene H. Sharpe, Jay R. Thiagarajah, Jonathan C. Kagan

Correspondence

charles.evavold@childrens.harvard.edu (C.L.E.), jonathan.kagan@childrens.harvard. edu (J.C.K.)

In brief

The Ragulator-Rag complex is required for the oligomerization of gasdermin D at the plasma membrane and for pore formation and pyroptosis in macrophages.

Highlights

- The Ragulator-Rag-mTORC1 pathway is required for pyroptosis induced by gasdermin D

- Ragulator-Rag promotes gasdermin D oligomerization but not membrane localization

- Ragulator-Rag promotes reactive oxygen species (ROS) production in macrophages

- ROS promotes gasdermin D oligomerization, pore formation, and pyroptosis

CellPress

Article

Control of gasdermin D oligomerization and pyroptosis by the Ragulator-Rag-mTORC1 pathway

Charles L. Evavold,[1,7,*] Iva Hafner-Bratkovič,[1,2,3,7] Pascal Devant,[1] Jasmin M. D'Andrea,[4,5] Elsy M. Ngwa,[1] Elvira Boršić,[2] John G. Doench,[6] Martin W. LaFleur,[4,5] Arlene H. Sharpe,[4,5,6] Jay R. Thiagarajah,[1] and Jonathan C. Kagan[1,8,*]

[1]Division of Gastroenterology, Boston Children's Hospital and Harvard Medical School, 300 Longwood Avenue, Boston, MA 02115, USA
[2]Department of Synthetic Biology and Immunology, National Institute of Chemistry, Hajdrihova 19, 1000 Ljubljana, Slovenia
[3]EN-FIST Centre of Excellence, Trg Osvobodilne fronte 13, 1000 Ljubljana, Slovenia
[4]Department of Microbiology and Immunobiology, Harvard Medical School, Boston, MA 02115, USA
[5]Evergrande Center for Immunological Diseases, Harvard Medical School and Brigham and Women's Hospital, Boston, MA 02115, USA
[6]Broad Institute of Massachusetts Institute of Technology and Harvard, Cambridge, MA 02142, USA
[7]These authors contributed equally
[8]Lead contact
*Correspondence: charles.evavold@childrens.harvard.edu (C.L.E.), jonathan.kagan@childrens.harvard.edu (J.C.K.)
https://doi.org/10.1016/j.cell.2021.06.028

SUMMARY

The process of pyroptosis is mediated by inflammasomes and a downstream effector known as gasdermin D (GSDMD). Upon cleavage by inflammasome-associated caspases, the N-terminal domain of GSDMD forms membrane pores that promote cytolysis. Numerous proteins promote GSDMD cleavage, but none are known to be required for pore formation after GSDMD cleavage. Herein, we report a forward genetic screen that identified the Ragulator-Rag complex as being necessary for GSDMD pore formation and pyroptosis in macrophages. Mechanistic analysis revealed that Ragulator-Rag is not required for GSDMD cleavage upon inflammasome activation but rather promotes GSDMD oligomerization in the plasma membrane. Defects in GSDMD oligomerization and pore formation can be rescued by mitochondrial poisons that stimulate reactive oxygen species (ROS) production, and ROS modulation impacts the ability of inflammasome pathways to promote pore formation downstream of GSDMD cleavage. These findings reveal an unexpected link between key regulators of immunity (inflammasome-GSDMD) and metabolism (Ragulator-Rag).

INTRODUCTION

The link between cell death and inflammation has long been recognized, with certain death processes inducing immuno-suppressive responses (e.g., apoptosis) and others inducing inflammatory responses (e.g., pyroptosis). Central to the inflammatory process of pyroptosis is the protein gasdermin D (GSDMD) (Kayagaki et al., 2015; Shi et al., 2015), which forms pores in the plasma membrane of cells that can result in lysis and the release of intracellular inflammatory mediators (Kovacs and Miao, 2017; Lieberman et al., 2019). Among these inflammatory mediators are interleukin (IL)-1 family cytokines (Dinarello, 2018), which are cytosolic proteins that can be released from living (Evavold et al., 2018; Heilig et al., 2018) or pyroptotic (Kayagaki et al., 2015; Shi et al., 2015) cells after GSDMD pore formation. In contrast to their pyroptotic counterparts, apoptotic cells typically maintain plasma membrane integrity and therefore do not release inflammatory mediators. Distinctions in plasma membrane integrity therefore (in part) explain inflammatory or non-inflammatory consequences of the different processes of cell death.

Two known mechanisms explain GSDMD pore formation and inflammation. The first mechanism involves the actions of inflammasomes, which are supramolecular organizing centers that function as the subcellular sites of caspase-1 activation

(Chan and Schroder, 2020). Caspase-1 is a dormant enzyme in resting cells. Upon infection or select disruptions of cellular homeostasis, inflammasomes are assembled in the cytosol that recruit and activate caspase-1. This enzyme cleaves GSDMD into two fragments. The N-terminal fragment oligomerizes and inserts into the plasma membrane where it forms pores of 10–20 nm in inner diameter (Aglietti et al., 2016; Ding et al., 2016; Liu et al., 2016; Ruan et al., 2018; Sborgi et al., 2016). The second means by which pyroptosis is induced is by the actions of murine caspase-11 (or caspase-4 and -5 in humans). The catalytic activity of these caspases is not stimulated by recruitment into inflammasomes. Rather, catalytic activity is stimulated upon binding to bacterial lipopolysaccharides (LPS) (Hagar et al., 2013; Kayagaki et al., 2013; Shi et al., 2014). Upon LPS binding, active caspase-11 cleaves GSDMD in a manner similar to caspase-1 (Wang et al., 2020), leading to pore formation and pyroptosis (Aglietti et al., 2016; Kayagaki et al., 2015; Liu et al., 2016; Shi et al., 2015). Caspase-8 also cleaves GSDMD to induce pyroptosis in certain contexts (Orning et al., 2018; Sarhan et al., 2018).

Despite the importance of GSDMD in pyroptosis, mechanisms regulating its activity are largely focused on upstream factors that influence its cleavage. For example, genetic deficiencies in components of inflammasomes (e.g., NLRP3 or ASC) prevent
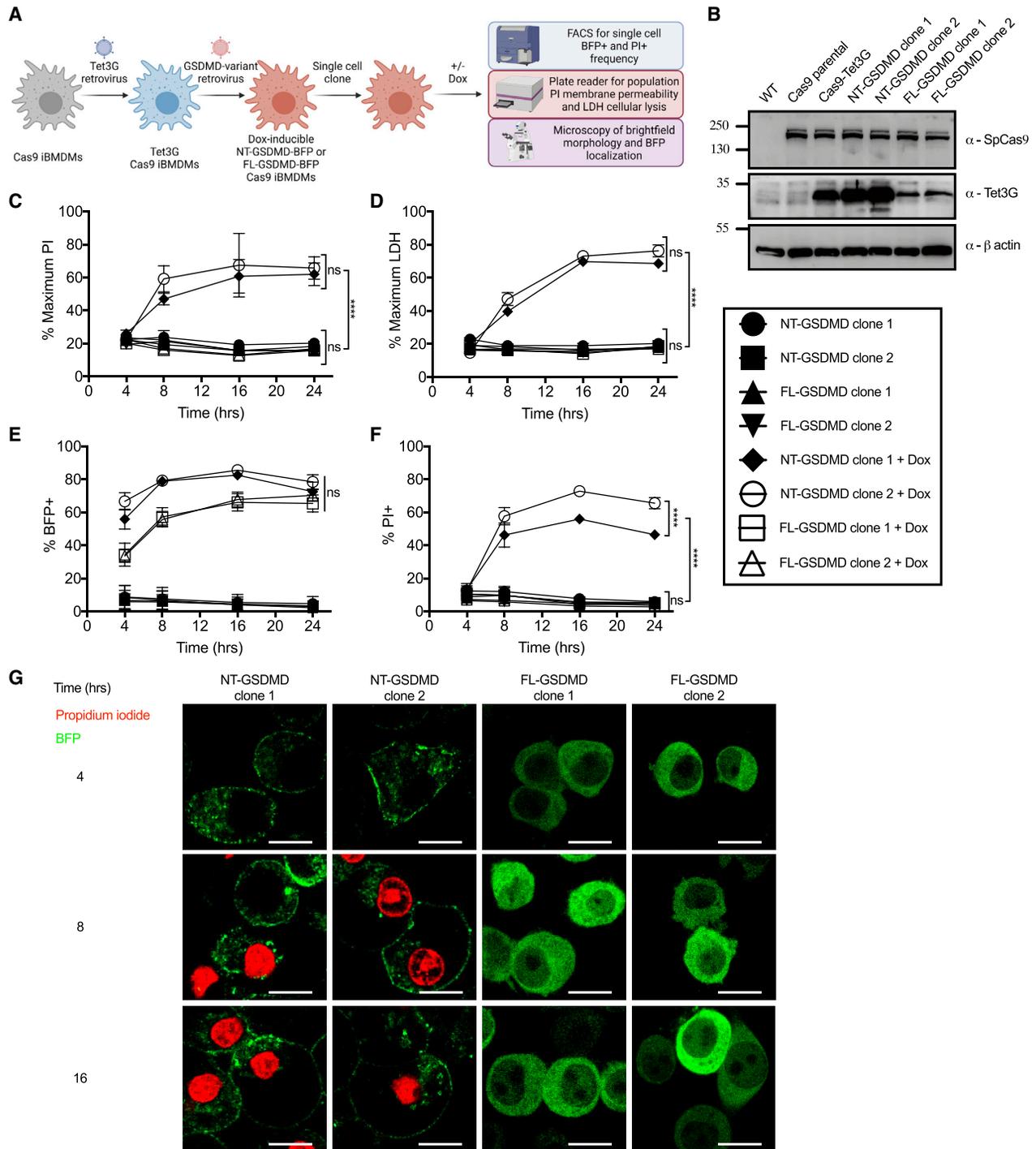
Figure 1. Engineered macrophages model pyroptosis through expression of the GSDMD N-terminal domain

(A) Retroviral transduction workflow to generate Tet3G transactivator-expressing Dox-inducible fluorescently tagged variants of GSDMD in iBMDMs from the Cas9 knockin mouse and downstream characterization.

(B) Western blot of stable Cas9 expression in parental and progeny iBMDMs and stable expression of Tet3G transactivator in progeny iBMDM clones with β-actin loading control.

(C) Kinetic analysis of PI uptake by plate reader to measure bulk membrane permeability in populations of uninduced or Dox-induced (0.5 μg/mL) cells expressing NT-GSDMD-BFP or FL-GSDMD-BFP.

(D) Time-course endpoint analysis of LDH release into cell-free supernatants to measure cell lysis in populations of uninduced or Dox-induced (0.5 μg/mL) cells expressing NT-GSDMD-BFP or FL-GSDMD-BFP.

(legend continued on next page)

caspase-1 activation, resulting in inefficient GSDMD cleavage and defects in pyroptosis. Moreover, certain stimuli and cell types may differentially impact the magnitude and duration of caspase activation, with a direct effect on the rate of GSDMD cleavage and pore formation (Boucher et al., 2018; Chen et al., 2014). TCA cycle intermediates modify a reactive cysteine within GSDMD resulting in reduced cleavage and pore formation (Humphries et al., 2020). While the above-mentioned mechanisms of regulation are diverse, they all operate upstream of GSDMD cleavage. Whether factors exist that promote pore formation at the plasma membrane, after GSDMD cleavage has occurred, is less clear.

In this study, we sought to fill this gap in our knowledge by performing a genome-wide genetic screen to identify factors which are required for pore-forming activity at the plasma membrane downstream of GSDMD cleavage. We identified components of the Ragulator-Rag complex, a mediator of mTOR activities, as necessary for GSDMD pore-forming activity in macrophages. Subsequent analysis revealed that the Ragulator-Rag complex controls mTORC1-dependent events that operate downstream of GSDMD cleavage to promote GSDMD oligomerization and pore formation, by a process mediated by mitochondrial reactive oxygen species (ROS). These studies therefore provide a link between key metabolic and cell-death regulators to control pyroptosis.

RESULTS

An experimental platform that bypasses natural regulatory mechanisms to specifically stimulate GSDMD pore-forming activity

We created a genetic screening system to identify genes that act after GSDMD cleavage to promote pore formation and pyroptosis. This goal was accomplished by taking advantage of the fact that the expression of the N-terminal caspase-cleavage product of GSDMD is sufficient to induce pore formation in the plasma membrane (Kayagaki et al., 2015; Shi et al., 2015). Thus, expression of the N-terminal GSDMD fragment (NT-GSDMD) bypasses upstream regulatory events that naturally lead to pyroptosis.

Using immortalized bone-marrow-derived macrophages (iBMDMs) from Cas9-expressing mice, we stably expressed the Tet3G transactivator, which enabled the doxycycline (Dox)-inducible expression of transgenes encoding NT-GSDMD and full-length GSDMD (FL-GSDMD) both of which contained a C-terminal BFP tag (Figures 1A and 1B). We utilized a variant of the NT-GSDMD that contains an I105N mutation, as this mutant is more readily detected within cells than its wild-type (WT) counterpart (Aglietti et al., 2016).

We characterized the ability of NT-GSDMD and FL-GSDMD to induce plasma membrane pore formation and lysis after Dox treatment. Pore formation was assessed by treatment with propidium iodide (PI), a membrane impermeable dye that can pass

through GSDMD pores and enter cells. PI fluoresces upon binding to intracellular nucleic acids. Cytolysis was assessed by the release of the cytosolic enzyme lactate dehydrogenase (LDH) into the extracellular space. LDH is only released from cells post-lysis (Evavold et al., 2018).

Dox-mediated induction of NT-GSDMD, but not FL-GSDMD, resulted in pore formation and cell lysis, as revealed by population-level PI fluorescence and LDH release (Figures 1C and 1D). Induction of both GSDMD transgenes corresponded with BFP induction, as evidenced by an increase in frequency of BFP positive cells over time in a Dox-dependent manner (Figure 1E). Flow cytometry demonstrated that the frequency of PI positive cells increased over time in a Dox-dependent manner for cells expressing NT-GSDMD (Figure 1F). Confocal microscopy demonstrated that NT-GSDMD is localized primarily to the plasma membrane, whereas FL-GSDMD was distributed throughout the cell (Figure 1G). Live-cell microscopy demonstrated that PI staining occurred in a time-dependent manner in cells expressing the NT-GSDMD but not in cells expressing FL-GSDMD (Figure 1G).

Finally, we sought to determine whether NT-GSDMD-mediated pyroptosis induced by our Dox system was impacted by the endogenous inflammasome machinery within the cell. We found that Dox-induced pore-forming activity of NT-GSDMD remained intact in LPS primed or unprimed cells that were treated with the NLRP3-specific inhibitor MCC950 (Coll et al., 2019; Tapia-Abellán et al., 2019) (Figures S1A and S1B). In parallel stimulations, MCC950 prevented PI uptake and LDH release that was induced by the treatment of LPS-primed cells with the NLRP3 agonist Nigericin (Figures S1C and S1D). These collective results establish an experimental system to induce GSDMD pore-forming activity directly, independent of inflammasomes, thus enabling the identification of factors that specifically mediate these events.

A forward genetic screen identifies the Ragulator-Rag complex as necessary for GSDMD pore formation

To identify genes that regulate GSDMD pore formation, a genome-wide CRISPR-Cas9 screen was performed. iBMDMs encoding NT-GSDMD were verified to produce similar amounts of Cas9 protein, as compared to their parental line (Figure 1B). We lentivirally transduced iBMDMs encoding NT-GSDMD with the Brie genome-wide single-guide RNA (sgRNA) library (Doench et al., 2016). Cells were treated with Dox to induce NT-GSDMD expression for 16 h and then stained with PI to label cells containing GSDMD pores. The top 15% of cells that were BFP-positive and PI-negative were isolated by fluorescence-activated cell sorting (FACS). These cells expressed the NT-GSDMD transgene (as identified by the BFP tag) but have not formed pores. These cells were therefore predicted to contain mutations in genes that promote GSDMD pore formation.

After PCR amplification of sgRNA sequences from genomic DNA, and subsequent next-generation sequencing, the

---

(E and F) Time-course endpoint analysis by flow cytometry of the frequency of BFP⁺ (E) or PI⁺ cells (F) using uninduced or Dox-induced (0.5 μg/mL) cells expressing NT-GSDMD-BFP or FL-GSDMD-BFP.

(G) Time-course live-cell imaging of Dox-induced cells expressing NT-GSDMD-BFP or FL-GSDMD-BFP noting localization of BFP signal and PI uptake. Scale bar indicates 10 μm.

All quantification represents the mean and SEM of three independent experiments. Two-way ANOVA was used for analysis. See also Figure S1.
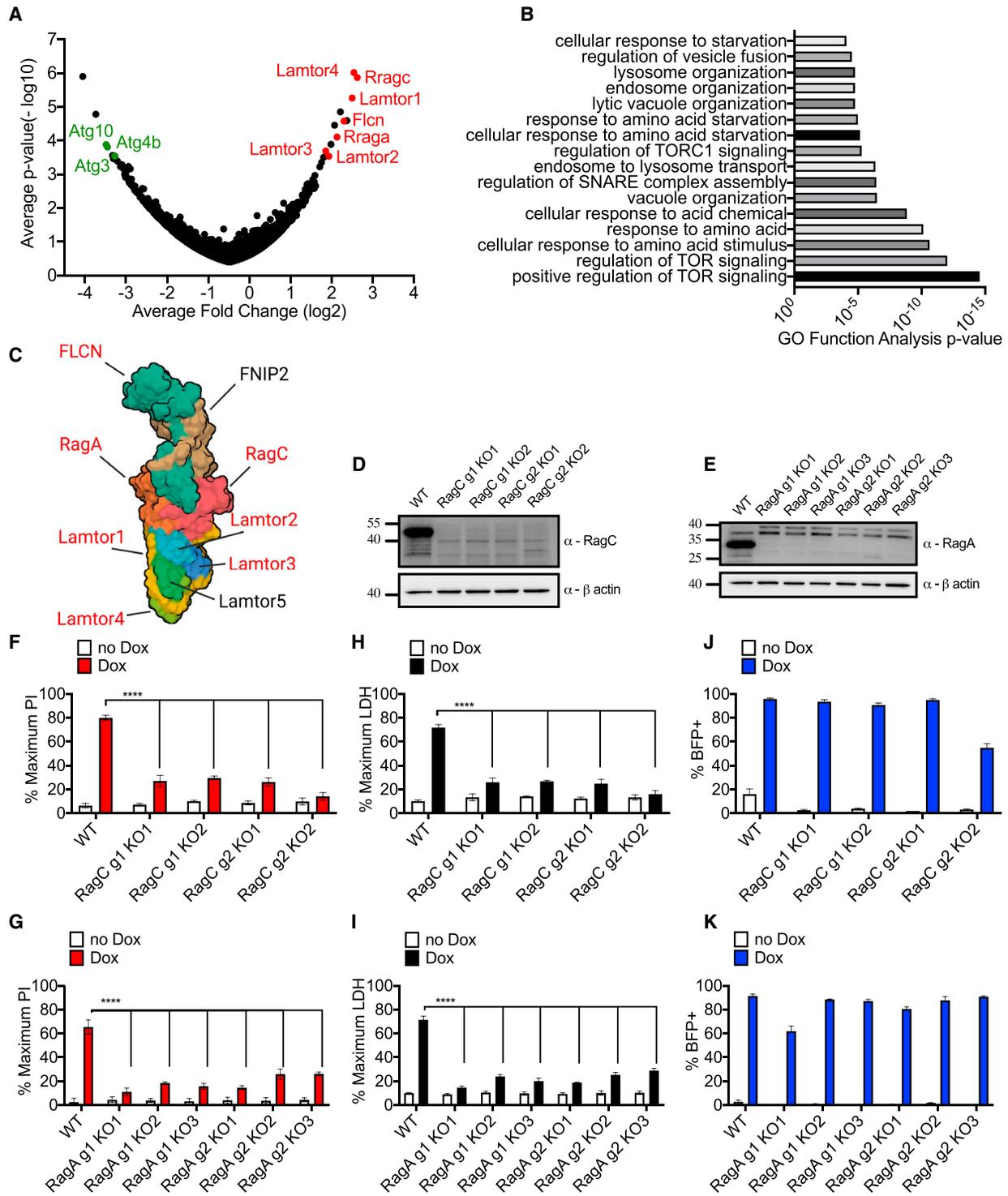
Figure 2. Analysis of survivor cells sgRNA enrichment and validation of screen hits

(A) Hypergeometric analysis of log-normalized guide abundance of survivor cells subtracted by the log-normalized abundance of input cells plotted as gene-level average p-value versus gene-level average LFC.

(B) Gene ontology functional annotation enrichment analysis for ranked hit list using GOrilla web analysis tool.

(C) Cryo-EM structure of the Ragulator-Rag complex cartoon schematic with top hits identified from CRISPR screen highlighted in red.

(D and E) Western blot of RagC (D) or RagA (E) protein ablation comparing empty vector transduced or cells expressing sgRNA guides targeting RagC and RagA.

(legend continued on next page)

log-normalized sgRNA abundance from the input sample was subtracted from the log-normalized sgRNA abundance of BFP-positive survivors. Using hypergeometric analysis, average p-values were generated and plotted against average log-fold change (LFC) at the gene level (Figure 2A). Gene ontology analysis of the rank list of genes from most positive LFC to most negative LFC identified functional annotations that were enriched in our dataset. The most significant function was attributed to positive regulation of mTOR signaling (Figure 2B). Many of the genes with the highest positive LFC and most significant p-values were part of the Ragulator-Rag complex (Figures 2A and 2C). Highlighted potential positive regulators of GSDMD pore formation are indicated in red on the volcano plot (Figure 2A) and on a schematized cryoelectron microscopy (cryo-EM) structure of this protein complex (Figure 2C) (Shen et al., 2019). Specifically, we identified the GTPases RagA and RagC and their functionally related GTPase activating protein (GAP) FLCN, as well as the major components of the Ragulator complex—Lamtor-1, -2, -3, -4. These proteins are best known for their metabolic activities (Liu and Sabatini, 2020), but a role in GSDMD activities is unprecedented. We also noted that several of the genes with the highest negative LFC and most significant p values correspond to members of the autophagy pathway, including E2-like conjugating enzymes Atg10 and Atg3 and cysteine protease Atg4b. Highlighted potential negative regulators of GSDMD pores are indicated in green on the volcano plot (Figure 2A). Recent work has begun to uncover that the Ragulator-Rag complex can serve as an organelle quality-control mechanism for lysosomes and mitochondria that likely operates through induction of autophagy (Condon et al., 2021; Jia et al., 2018). Based on the concordance of biological processes between our potential positive and negative regulators of GSDMD pore formation, we focused our subsequent studies on the functions of Ragulator-Rag in pyroptosis.

To validate our top screen hits, we targeted specific components of the Ragulator-Rag complex for genetic ablation. Using independent sgRNAs and single-cell clones from each sgRNA, we ablated protein production of RagA and RagC, as compared to empty vector transduced cells (Figures 2D and 2E). As expected (Rogala et al., 2019), ablation of RagA and RagC reduced activity of mTOR, based on reduced phosphorylation of S6 Kinase (S6K) (Figure S2A). Phospho-S6K abundance was not altered by Dox induction (Figure S2A). After induction of NT-GSDMD, RagA- or RagC-deficient clones displayed defects in PI staining (Figures 2F and 2G) and LDH release (Figures 2H and 2I). The percentage of BFP-positive cells was comparable between Rag-deficient cells and cells containing an empty vector control (Figures 2J and 2K). Live-cell imaging verified these results, as empty vector control cells displayed high frequencies of PI uptake and disintegration of morphology after NT-GSDMD expression (Video S1). In contrast, a low frequency of PI uptake and maintenance of cellular morphology was observed in two

different lines of RagA-deficient iBMDMs (Videos S2 and S3). These data validate the importance of Ragulator-Rag in GSDMD-mediated pore formation and pyroptosis.

RagA regulates NT-GSDMD pore activity in primary murine cells and a human cell line

To explore the role of RagA in inflammasome signaling in primary immune cells, we employed the chimeric immune editing (CHIME) protocol to create control untargeted and RagA targeted bone-marrow chimeras to ablate genes of interest in hematopoietic cells (LaFleur et al., 2019). We depleted the RagA protein in primary BMDMs derived from these mice, as compared to control untargeted BMDMs (Figure 3A). To activate inflammasome signaling in unprimed cells, we treated BMDMs with the synthetic toxin system consisting of anthrax protective antigen (PA) and the fusion protein of anthrax lethal factor with bacterial flagellin (LFn-Fla) that is collectively termed FlaTox (von Moltke et al., 2012; Zhao et al., 2011). Delivery of flagellin to the cytosol activates the NAIP-NLRC4 inflammasome, caspase-1, and subsequent GSDMD cleavage (Kofoed and Vance, 2011; Zhao et al., 2011). WT and RagA-deficient BMDMs displayed similar GSDMD cleavage after FlaTox administration, suggesting that RagA does not affect inflammasome activities (Figure 3A). In contrast, RagA depletion resulted in diminished pore formation, as observed by the frequency of PI positive cells (Figure 3B), or population-level PI fluorescence (Figure S3A). Similarly, bulk populations of primary splenocytes from WT bone-marrow chimeras treated with FlaTox displayed CD11b$^+$ phagocyte depletion, as compared to LFn-Fla treated splenocytes from the same mice (Figure 3C). In contrast, splenocytes from RagA-deficient bone-marrow chimeras demonstrated resistance to CD11b$^+$ depletion by FlaTox (Figure 3C). These data in primary BMDMs and splenic phagocytes support the importance of RagA in GSDMD-mediated pyroptosis.

To extend our analysis of Ragulator-Rag control of GSDMD pore formation and pyroptosis, we examined human GSDMD alleles in human cells. We analyzed the ability of GSDMD to form pores in WT and RagA/B double KO (DKO) 293T cells (Rogala et al., 2019). In addition to the caspase cleavage product of human GSDMD (hNT-GSDMD), we examined a destabilized full-length variant GSDMD L290D, which can form pores as a full-length protein (Liu et al., 2019). We found that GSDMD-mediated PI uptake and LDH release was diminished in RagA/B DKO cells, as compared to WT cells (Figures 3D and 3E). No genotype-specific differences in GSDMD expression were observed (Figure 3F). In addition, RagA/B DKO cells were not generally defective for immune signaling events, as these cells were not deficient in MyD88 L265P-induced nuclear factor κB (NF-κB) reporter activation (Figure 3G).

mTOR activity is required for NT-GSDMD pore formation
Ragulator-Rag is best known for its functions in mTOR regulation. To determine the role of mTOR in GSDMD pore formation,

---

(F and G) PI uptake analysis of cells of the genotypes indicated, left uninduced or Dox-induced (2 μg/mL) for 16 h.

(H and I) LDH release from cells of the genotypes indicated, left uninduced or Dox-induced (2 μg/mL) for 16 h.

(J and K) Frequency of BFP$^+$ cells by flow cytometry of cells of the genotypes indicated, left uninduced or Dox-induced (2 μg/mL) for 16 h.

All quantification represents the mean and SEM of three independent experiments. Two-way ANOVA was used for analysis. See also Figure S2.
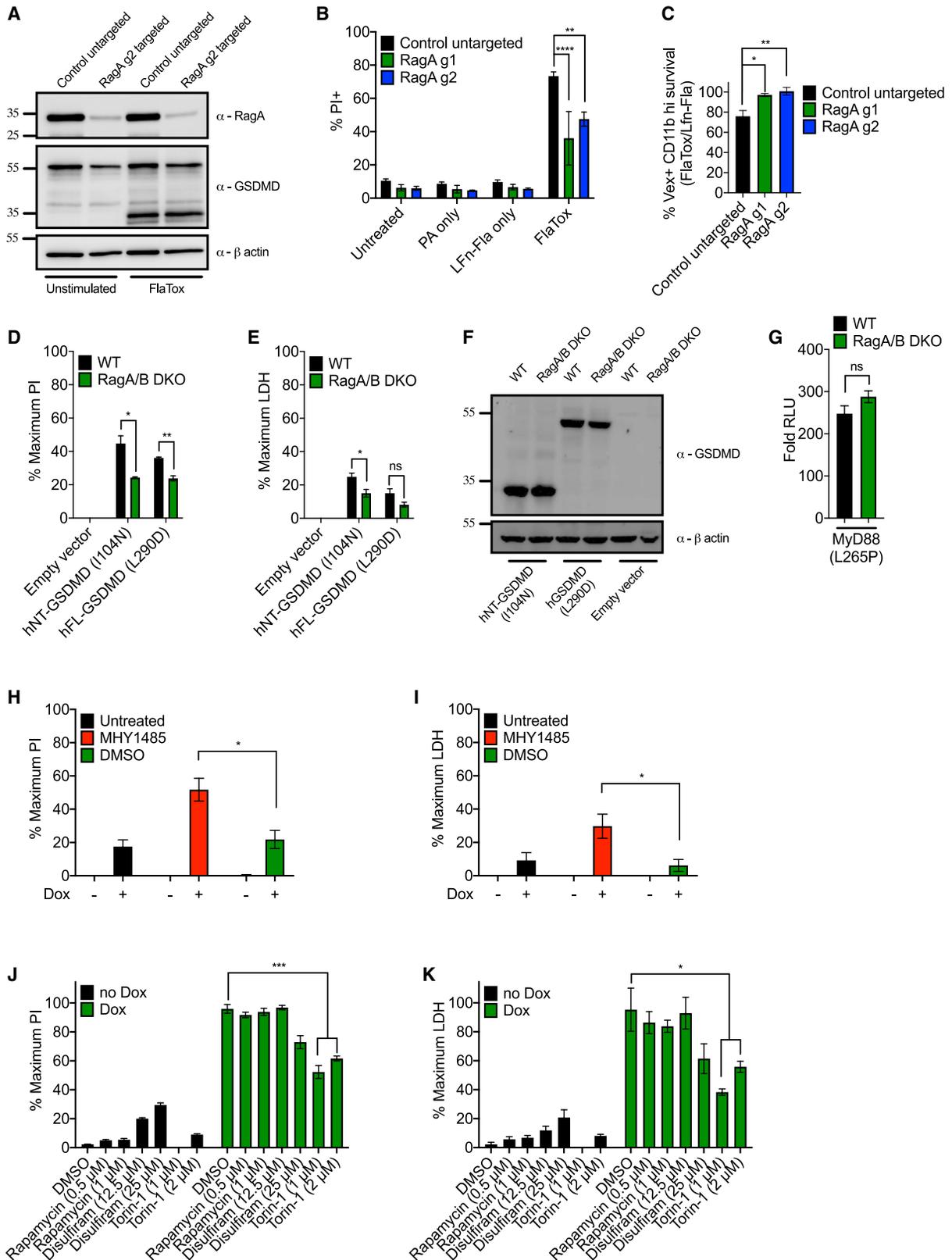
(legend on next page)

we examined chemical agonists or inhibitors of mTOR activity. To exclude complications in data interpretation associated with known mTOR functions upstream of inflammasome activation (Moon et al., 2015), we used Dox-inducible cells for this analysis. We found that the mTOR activator MHY1485 promoted GSDMD pore formation, as treatments with this chemical at the time of Dox treatment led to an increase in PI uptake and LDH release, as compared to untreated controls (Figures 3H and 3I). We note that because we were examining a boost in pore formation (not an inhibition) by MHY1485, we used a time point where cells treated with Dox contained evidence of <20% pores. The mTOR inhibitor Torin-1 had the opposite effect from MHY1485, in that Torin-1 suppressed NT-GSDMD-induced PI uptake and LDH release (Figures 3J and 3K). Although incomplete, the inhibitory effect of Torin-1 on GSDMD pore formation was comparable to that observed with the GSDMD inhibitor disulfiram (Hu et al., 2020). In contrast to the inhibition of GSDMD pore activity with Torin-1 treatment, the mTOR inhibitor rapamycin, which is not as effective as Torin-1 (Thoreen et al., 2009), was unable to prevent GSDMD-induced pore-forming activities (Figures 3J and 3K). Rapamycin and Torin-1 suppressed phosphorylation of the mTOR target S6K (Figure S3B). No effects of these inhibitors on the expression of GSDMD were observed (Figure S3B). The lack of phenotype with rapamycin on GSDMD pore formation, while unexplained, may be related to observations that this drug does not affect all branches of mTORC1 signaling equally (Howell and Manning, 2011).

To better define the role of mTOR in GSDMD activities, we focused on the two protein complexes that harbor this enzyme, mTORC1 and mTORC2. mTORC1 is controlled by several upstream pathways, including the Ragulator-Rag complex in response to amino acid availability (Sancak et al., 2010). To test whether mTORC1 stimulation by amino acids affects NT-GSDMD activities, we controlled GSDMD cleavage through co-expression of a small-molecule dimerizable caspase-1 and hFL-GSDMD in 293T cells. After amino acid starvation, dimerizer was added to cells that were either stimulated with amino acids or not. Amino acid treatments led to an increase in mTORC1 activity, as observed by increased S6K phosphorylation (Figure S3C). While addition of dimerizer induced comparable reduction in FL-GSDMD band intensity, indicating similar GSDMD cleavage (Figure S3C), pyroptosis was most increased in amino acid stimulation conditions (Figure S3D). Thus, stimulation of mTORC1 activities promoted GSDMD pore-forming activity.

Tuberous sclerosis complex is an endogenous negative regulator of mTORC1 activation (Yang et al., 2021). We found that overexpression of TSC-1, a component of tuberous sclerosis complex, decreased NT-GSDMD-induced PI uptake and LDH release (Figures 4A and 4B). NT-GSDMD protein abundance was unaffected by TSC-1 overexpression (Figure 4C). In addition, TSC-1 overexpression did not affect NF-κB reporter activation by MyD88 L265P (Figure 4D). Thus, several strategies of mTOR modulation impact GSDMD pore-forming activity in a manner consistent with a role of mTORC1 in promoting pyroptosis.

mTORC1, but not mTORC2, is required for GSDMD pore-forming activity and pyroptosis

To determine the relative roles of mTORC1 and mTORC2 in pyroptosis, we examined the function of the mTORC1 component Raptor and the mTORC2 component Rictor in iBMDMs. iBMDMs were generated from mice encoding CRE recombinase whose expression is driven by the macrophage-specific LysM promoter (hereafter referred to as LysM-CRE iBMDMs). Similarly, iBMDMs were derived from mice dually encoding LysM-CRE and floxed alleles of Raptor or Rictor (hereafter referred to as Raptor-deficient or Rictor-deficient iBMDMs). We verified protein ablation in Raptor- and Rictor-deficient iBMDMs (Figure S4A). These cells were subjected to stimulations that activate pathways leading to cleavage and pore formation by endogenous GSDMD.

We first focused on GSDMD pore-forming activity that is stimulated upon detection of cytosolic LPS by caspase-11. LysM-CRE WT iBMDMs were primed with type I interferon-β (IFN-β) to induce caspase-11 expression and then electroporated with PBS or LPS to activate caspase-11. Under these conditions, we observed LPS-induced pyroptosis of LysM-CRE WT and Rictor-deficient iBMDMs, as evidenced by PI incorporation and LDH release (Figures 4E and 4F). In contrast, Raptor-deficient cells were defective for LPS-induced pore formation and lysis (Figures 4E and 4F).

Figure 3. The role of Ragulator-Rag and mTOR activity in NT-GSDMD pore formation

(A) Western blot of RagA and GSDMD cleavage in WT control untargeted and RagA targeted primary BMDMs after 1 h of FlaTox treatment with β-actin loading control.

(B) Frequency of PI+ cells by flow cytometry of WT and RagA targeted primary BMDMs after 1 h of FlaTox treatment.

(C) Ratio of depletion of Vex+, CD11b high splenocytes after 1 h FlaTox treatment over LFn-Fla alone treatment.

(D and E) WT and RagA/B DKO 293T cells were transfected with plasmids encoding hGSDMD variants and normalized PI fluorescence (D) and cell-free supernatant LDH activity (E) were analyzed 20 h after transfection.

(F) Western blot of hGSDMD variants in transfected WT and RagA/B DKO 293T cells.

(G) MyD88 L265P-driven NF-κB reporter activity in WT and RagA/B DKO 293T cells by dual-luciferase system 24 h after transfection. Response of MyD88 L265P-transfected cells over empty vector-transfected cells is shown.

(H and I) Dox-inducible NT-GSDMD-BFP iBMDMs were treated with MHY1485 (10 μM) and Dox (0.5 μg/mL). Normalized PI fluorescence (H) and LDH activity in supernatants (I) were analyzed 6 h later.

(J and K) Dox-inducible NT-GSDMD-BFP iBMDMs were treated with different compounds and Dox (0.5 μg/mL). DMSO dose corresponds to DMSO content present in 2 μM Torin-1 samples. Normalized PI fluorescence (J) and extracellular LDH activity (K) were analyzed 14 h later.

Blots (A and F) are representative of two independent experiments. Means and SEM of three (B, C, D, E, G, J, and K) or four (H and I) independent experiments are shown. An unpaired two-tailed t test was used for pairwise comparison (D, E, G, H, and I). One-way ANOVA (C) and two-way ANOVA (B, J, and K) were used for analysis. See also Figure S3.

A

% Maximum PI

TSC-1

hNT-GSDMD
(I104N)

***

B

LDH release (%)

TSC-1

hNT-GSDMD
(I104N)

****

C

hNT-GSDMD
(I104N) − + + +
TSC1 − − ◢

130 —   α - HA (TSC1)

35 —   α - GSDMD

55 —   α - β actin

D

Fold RLU

ns

TSC-1

MyD88
(L265P)

E

% Maximum PI

□ PBS electro
■ LPS electro

*

****

ns

LysM CRE (WT)
LysM CRE (Rictor deficient)
LysM CRE (Raptor deficient)
LysM CRE (WT)
LysM CRE (Rictor deficient)
LysM CRE (Raptor deficient)

F

% Maximum LDH

□ PBS electro
■ LPS electro

ns

****

ns

LysM CRE (WT)
LysM CRE (Rictor deficient)
LysM CRE (Raptor deficient)
LysM CRE (WT)
LysM CRE (Rictor deficient)
LysM CRE (Raptor deficient)

G

%Annexin-V+, 7-AAD+

■ no STS
▨ STS

ns

ns

LysM CRE (WT)
LysM CRE (Rictor deficient)
LysM CRE (Raptor deficient)
LysM CRE (WT)
LysM CRE (Rictor deficient)
LysM CRE (Raptor deficient)

H

% Maximum PI

■ LysM-CRE
■ LysM-CRE (Rictor deficient)
■ LysM-CRE (Raptor deficient)
■ WT
■ NLRP3 deficient
□ GSDMD deficient

ns

*

****

Unstimulated   Salmonella

I

% Maximum LDH

■ LysM-CRE
■ LysM-CRE (Rictor deficient)
■ LysM-CRE (Raptor deficient)
■ WT
■ NLRP3 deficient
□ GSDMD deficient

ns

*

****

Unstimulated   Salmonella

J

LysM CRE (WT)
LysM CRE (Rictor deficient)
LysM CRE (Raptor deficient)
LysM CRE (WT)
LysM CRE (Rictor deficient)
LysM CRE (Raptor deficient)

55 —
40 —   α - GSDMD
35 —

40 —   α - β actin

PBS electro   LPS electro

K

LysM CRE (WT)
LysM CRE (Rictor deficient)
LysM CRE (WT)
WT
NLRP3 deficient
GSDMD deficient
LysM CRE (WT)
LysM CRE (Rictor deficient)
LysM CRE (WT)
WT
NLRP3 deficient
GSDMD deficient

55 —
40 —   α - GSDMD
35 —

40 —   α - β actin

Unstimulated   Salmonella

(legend on next page)

To complement these studies, we replaced the IFN-β priming step with a priming step using LPS. As pro-IL-1β is upregulated by TLR4 signaling, we expanded our analysis to include IL-1β release after pyroptosis. LPS electroporation of LPS-primed LysM-CRE WT iBMDMs stimulated PI staining, LDH, and IL-1β release, all of which were reduced in Raptor-deficient cells (Figures S4B–S4D). In contrast, Rictor-deficient cells displayed no defects in PI staining or LDH release upon LPS electroporation (Figures S4B and S4C). Interestingly, whereas Raptor-deficient cells released less IL-1β than WT counterpart cells, Rictor-deficient cells released a greater amount of IL-1β than WT counterparts (Figure S4D). This increased secretion of IL-1β is likely attributed to increased pro-IL-1β expression after LPS priming in Rictor-deficient cells (Figure S4E). Thus, mTORC1 and mTORC2 have disparate functions in the pathways to pyroptosis. Live-cell imaging confirmed these findings, as most LysM-CRE WT iBMDMs (Video S4) and Rictor-deficient iBMDMs (Video S5) experienced PI uptake and disintegration of morphology after LPS electroporation. In contrast, fewer Raptor-deficient cells converted to PI positivity after LPS electroporation (Video S6). In contrast to the requirement of Raptor for pyroptosis, WT, Raptor-, and Rictor-deficient cells similarly committed to death upon treatment with the apoptosis-inducer staurosporine (STS) (Figure 4G).

To complement the above studies, we performed infections with *Salmonella enterica* serovar Typhimurium. *S.* Typhimurium infections activate inflammasome pathways mediated by caspase-11, NLRP3, and NAIP-NLRC4, all of which converge on GSDMD to induce pyroptosis (Broz et al., 2010; Franchi et al., 2006; Man et al., 2014). Within 1 h of infection, PI staining, and LDH release occurred in LysM-CRE WT and in C57BL/6J WT iBMDMs (Figures 4H and 4I). NLRP3 deficiency did not protect iBMDMs from pyroptosis during infection, whereas GSDMD-deficient cells were defective for these responses (Figures 4H and 4I). Notably, Raptor-deficient cells displayed lower PI staining and LDH release upon *S.* Typhimurium infection, as compared to Rictor-deficient or LysM-CRE WT cells (Figures 4H and 4I).

To determine the stage of the pyroptotic process Raptor is necessary to execute, we examined early and late events. An early event is the upregulation of caspase-11 induced by extracellular LPS or IFN-β (Rathinam et al., 2012). We found that the abundance of caspase-11 marginally differed when comparing LPS- or IFN-β-treated LysM-CRE WT iBMDMs to Raptor- and Rictor-deficient cells (Figures S4F and S4G). However, within unstimulated cells, caspase-11 abundance differed between these genotypes (Figures S4F and S4G). The significance of this phenotype is unclear. Thus, we sought to examine the question of cell priming in a functional manner. We reasoned that if there were functional differences associated with Raptor or Rictor deficiency, in terms of priming events, then cleavage of GSDMD should be impacted. To address this possibility, we monitored GSDMD cleavage after the stimulations described above. Raptor-deficient cells were not defective for GSDMD cleavage when IFN-β-primed cells were electroporated with LPS or when cells were infected with *S.* Typhimurium (Figures 4J and 4K). The Ragulator-Rag complex and its downstream effector mTORC1 therefore operate downstream of GSDMD cleavage to promote pore formation and pyroptosis.

RagA or RagC are not required for NT-GSDMD plasma membrane localization but are required for oligomerization and pore formation

To determine the mechanisms by which Ragulator-Rag-mTORC1 controls GSDMD pore formation, we examined the two primary GSDMD activities that occur post-cleavage—membrane localization and oligomerization (Ding et al., 2016; Liu et al., 2016).

We first investigated the trafficking of NT-GSDMD to the plasma membrane. WT cells displayed NT-GSDMD at the plasma membrane and many cells co-stained with PI (Figure 5A). RagA- and RagC-deficient cells also displayed NT-GSDMD at the cell surface yet stained negative for PI (Figure 5A). Similarly, biochemical fractionations revealed no defects in the localization of NT-GSDMD to membrane fractions in RagA- or RagC-deficient macrophages (Figure 5B). Thus, RagA and RagC do not control the localization or membrane binding properties of NT-GSDMD.

To examine GSDMD oligomerization, which correlates with pore formation, we used a protocol that distinguishes monomeric and oligomeric GSDMD. Specifically, NT-GSDMD oligomers (i.e., pores) are resistant to SDS destabilization unless a reducing agent is present (Liu et al., 2016). Using this principle, we subjected WT, RagA-deficient, and RagC-deficient cells to SDS lysis after Dox induction of NT-GSDMD. When no reducing

Figure 4. mTORC1 acts downstream of GSDMD cleavage to promote pore formation and pyroptosis

(A–C) HEK293 cells were co-transfected with plasmids encoding hNT-GSDMD (I104N) and TSC-1. Normalized PI fluorescence (A), extracellular LDH activity (B), and protein abundance (C) were analyzed 20 h post-transfection.

(D) MyD88 L265P-driven NF-κB dual-luciferase system response in HEK293 cells transfected with TSC-1 24 h after transfection. Response of MyD88 L265P-transfected cells over empty vector-transfected cells is shown.

(E and F) PI uptake (E) and LDH release assessment (F) of LysM-CRE WT, Rictor-deficient, and Raptor-deficient iBMDMs, primed with recombinant IFN-β for 3 h then electroporated with PBS or LPS.

(G) Frequency of Annexin-V and 7-AAD positive cells by flow cytometry from LysM-CRE WT, Rictor-deficient, and Raptor-deficient iBMDMs after 8 h of 1 μM staurosporine (STS) treatment.

(H and I) PI uptake (H) and LDH release (I) from LysM-CRE WT, Rictor-deficient, Raptor-deficient, C57/BL6J WT, NLRP3-deficient, and GSDMD-deficient iBMDMs, unstimulated or infected with *S.* Typhimurium at an MOI of 10 for 1 h.

(J) Western blot of the proteins indicated in LysM-CRE WT, Rictor-deficient, and Raptor-deficient iBMDMs, after these cells were primed with IFN-β and then electroporated with PBS or LPS.

(K) Western blot of the proteins indicated in LysM-CRE WT, Rictor-deficient, Raptor-deficient, C57/BL6J WT, NLRP3-deficient, and GSDMD-deficient iBMDMs, after these cells were unstimulated or infected with *S.* Typhimurium at an MOI of 10 for 1 h.

All quantifications represent mean and SEM of 3 independent experiments. Two-way ANOVA was used for analysis. See also Figure S4.

A

B

C

D

E

F

G
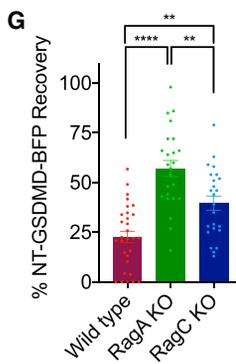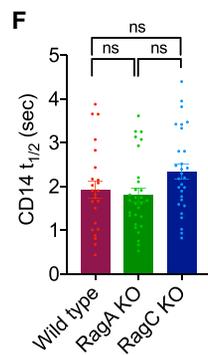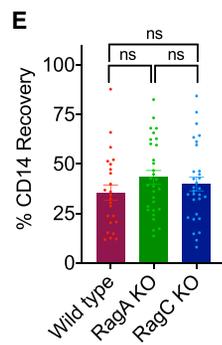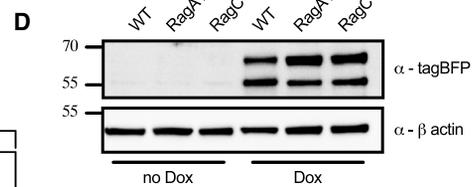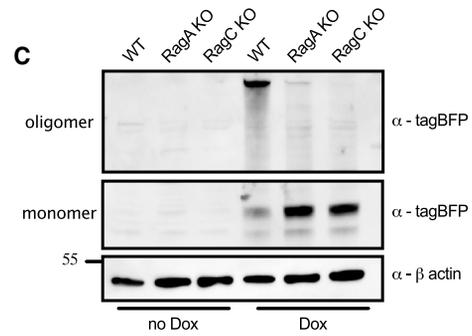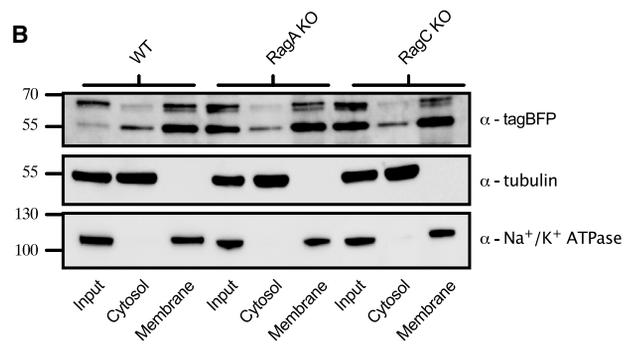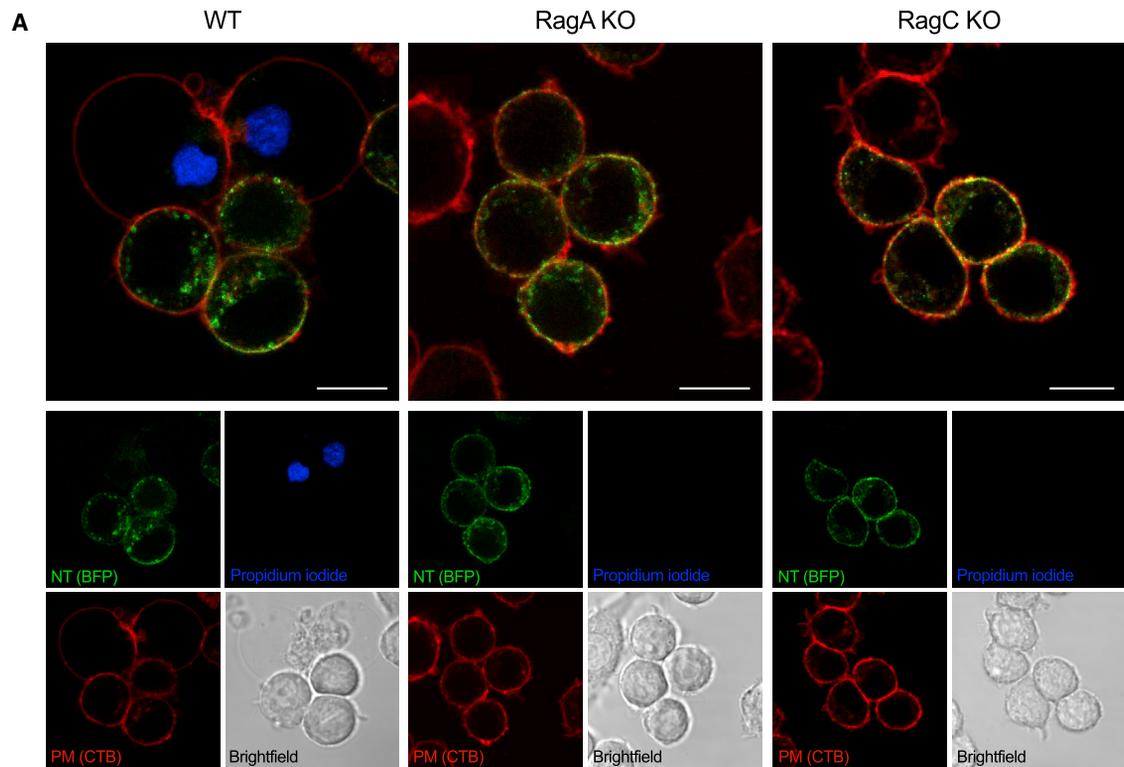
(legend on next page)

agent was added to the lysate, WT cells had mostly oligomerized NT-GSDMD (Figure 5C). In contrast, GSDMD oligomers were nearly absent from RagA- and RagC-deficient cells, yet NT-GSDMD monomeric species were abundant (Figure 5C). Treatment of the same lysates with the reducing agent TCEP dissociated the oligomerized NT-GSDMD in WT cells to the monomer phase (Figure 5D). These data demonstrate that RagA and RagC promote NT-GSDMD oligomerization.

We addressed whether membrane fluidity might underlie the defects in NT-GSDMD oligomerization in RagA- and RagC-deficient cells. Toward this end, we performed fluorescence recovery after photobleaching (FRAP) studies of the GPI-anchored membrane protein CD14 within the plasma membranes of WT, RagA-, and RagC-deficient macrophages. We noted no significant changes in either the fraction of recovery of fluorescence signal or half-life of recovery for the genotypes examined (Figures 5E and 5F). These results suggest that bulk membrane fluidity and diffusion of proteins within the plasma membrane are unaffected by RagA and RagC deficiency. We also performed FRAP studies on the plasma membrane localized BFP-tagged NT-GSDMD. Intriguingly, the fraction of BFP recovery was lower in WT cells than in RagA- and RagC-deficient cells (Figure 5G). This observation may represent *in situ* measurements of oligomerization of NT-GSDMD in the plasma membrane, as an oligomer would be expected to be more immobile than a monomer. These results support the conclusion that RagA and RagC regulate GSDMD pore formation because they control the necessary step of oligomerization in the plasma membrane.

Mitochondrial dysfunction and ROS mediate GSDMD oligomerization

To further define the link between Ragulator-Rag and GSDMD oligomerization, we considered another phenomenon co-incident with pore formation by GSDMD—the disruption of mitochondrial activities (de Vasconcelos et al., 2019; Kayagaki et al., 2021), which are also linked to Ragulator-Rag functions (Condon et al., 2021).

We quantified mitochondria abundance and membrane potential using MitoTracker and the potentiometric dye TMRM, along with PI positivity after Dox-induced NT-GSDMD expression. MitoTracker and TMRM staining was diminished in WT cells upon NT-GSDMD expression but was maintained upon NT-GSDMD expression in RagA-deficient cells (Figures S5A–S5G). In addition, mitochondrial ROS abundance increased in

WT cells, but not RagA-deficient cells, upon NT-GSDMD expression (Figure S5H). Similar findings were made when we measured total cellular ROS in WT, RagA-, and RagC-deficient cells using the reagent CellROX (Figure 6A). While diminished mitochondrial activities and increased ROS production may be expected to occur after pore formation, we were intrigued by the basal differences in ROS production observed. ROS levels were higher in resting WT cells than RagA- and RagC-deficient cells (Figure 6A), an observation that cannot be explained by NT-GSDMD pore activities. Thus, in cells with high ROS (WT cells), GSDMD pores are formed more efficiently than in cells with low ROS (Rag-deficient cells). We therefore determined whether the correlation between ROS and GSDMD pore formation might be causal.

To test whether ROS might affect the pore-forming ability of NT-GSDMD, we treated RagA- and RagC-deficient cells with increasing concentrations of H_2O_2. Upon addition of H_2O_2, RagA- and RagC-deficient cells displayed rescue of their oligomerization defect, as seen by increased NT-GSDMD oligomers (Figure 6B). Addition of reducing agent to these lysates reduced these oligomers back to the monomer phase, with the exception of a fraction of oligomers resisting reduction for the highest H_2O_2 dose (Figure 6C). The rescue of GSDMD oligomerization by H_2O_2 correlated with pore formation, as H_2O_2 treatment led to PI staining in RagA-deficient cells (Figure 6D). We excluded the possibility that H_2O_2-induced PI staining could be explained by ROS stimulating endogenous NLRP3 activities (Zhou et al., 2011), since NLRP3 inhibition by MCC950 did not impact PI staining (Figure 6D). Despite the observed restoration of NT-GSDMD pore-forming activities by H_2O_2, the extent of pore-formation rescue was incomplete, in particular, in the case of RagC-deficient cells (Figure 6D). We considered the possibility that an endogenous source of ROS (from mitochondria) may better impact NT-GSDMD pore-forming activity. Inhibition of the electron transport chain (ETC) can promote ROS production (Zhou et al., 2011). The complex I inhibitor Rotenone and complex III inhibitor Antimycin A alter the ETC in a manner that drives ROS production, whereas the complex II inhibitor TTFA does not induce ROS production (Zhou et al., 2011). Consistent with a role for ROS in GSDMD oligomerization, treatment with the mitochondrial ROS fluxing agents Rotenone and Antimycin A stimulated oligomerization of NT-GSDMD in RagA- and RagC-deficient cells (Figure 6E). In contrast, TTFA, which does not flux mitochondrial ROS, did not rescue NT-GSDMD oligomerization in RagA- and

Figure 5. RagA or RagC are not required for NT-GSDMD plasma membrane localization but are required for oligomerization and pore formation

(A) Confocal microscopy of NT-GSDMD-BFP (green) at 8 h post Dox induction (0.5 µg/mL) in WT, RagA KO, and RagC KO cells. Plasma membrane was labeled with CTB-AF647 (red), and membrane permeability was assessed by PI (blue). Scale bar indicates 10 µm.

(B) Western blot of NT-GSDMD-BFP from post-nuclear input, cytosolic, and bulk membrane fractions of WT, RagA KO, and RagC KO cells, after Dox induction (2 µg/mL) for 8 h. Tubulin represents a cytosol marker, and Na^+/K^+ ATPase represents a membrane marker.

(C and D) Western blot of NT-GSDMD-BFP from combined cell lysate and supernatant under non-reducing conditions (C) or reducing conditions (D) from WT, RagA KO, and RagC KO cells after Dox induction for 16 h.

(E) FRAP proportion of fluorescence recovery of CD14 labeled with PE-conjugated anti-CD14 antibody in WT, RagA KO, and RagC KO macrophages.

(F) FRAP half-life of fluorescence recovery of CD14 labled with PE-conjugated anti-CD14 antibody in WT, RagA KO, and RagC KO macrophages.

(G) FRAP proportion of fluorescence recovery of BFP signal from NT-GSDMD-BFP in WT, RagA KO, and RagC KO macrophages after Dox induction (2 µg/mL) for 8 h.

Each data point (E–G) represents parameters from a fitted FRAP curve from individual cells (n ≥ 24). One-way ANOVA was used for analysis.
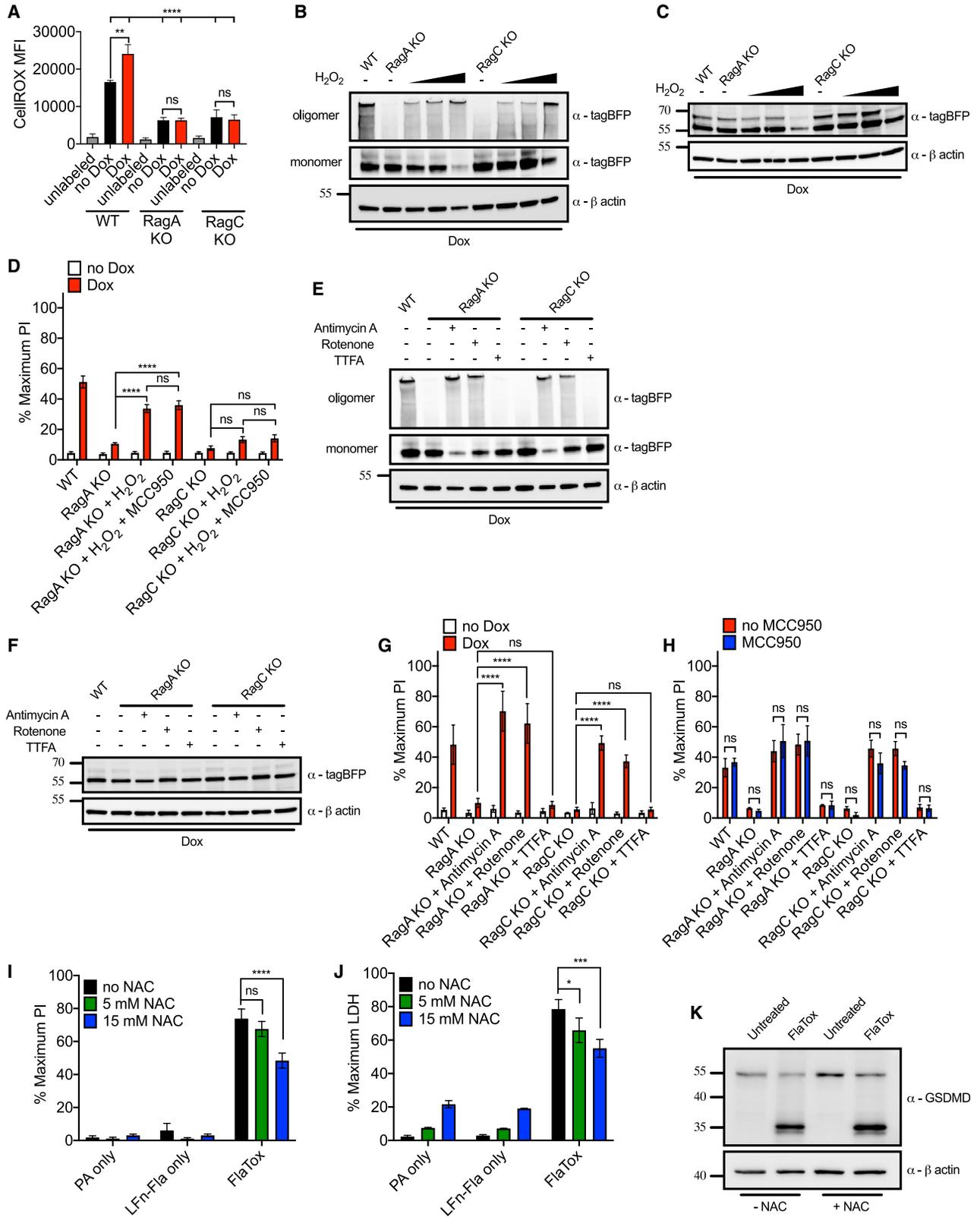
(legend on next page)

RagC-deficient cells. Addition of reducing agent to these lysates reduced oligomers into monomers and treatment with these mitochondrial poisons did not alter NT-GSDMD expression (Figure 6F). Importantly, we observed a complete rescue of NT-GSDMD pore-forming activities in RagA- and RagC-deficient cells, but only with mitochondrial disrupting agents that also rescued oligomerization (Figure 6G). All PI staining observed was NT-GSDMD-dependent, as PI staining was not observed in the absence of Dox treatments (Figure 6G). Finally, MCC950 did not impact PI staining in Rotentone or Antimycin A-treated RagA- or RagC-deficient cells expressing NT-GSDMD (Figure 6H). These data provide causal links between Ragulator-Rag, mitochondrial ROS, and NT-GSDMD oligomerization and pore formation. To investigate whether endogenous ROS promotes pyroptosis in natural inflammasome signaling, we again used the FlaTox system. We chose FlaTox (von Moltke et al., 2012) to avoid the roles of ROS in NLRP3 inflammasome activities (Bauernfeind et al., 2011; Dostert et al., 2008; Shimada et al., 2012; Zhou et al., 2011). Treatment of iBMDMs with increasing doses of the antioxidant NAC resulted in a reduction in pore formation and cytolysis (Figures 6I and 6J), while cleavage of GSDMD remained unchanged (Figure 6K). Mitochondrial health and ROS production therefore control GSDMD oligomerization and pore formation.

The protein Ninjurin-1 (NINJ1) controls pyroptosis at a late stage (Kayagaki et al., 2021). NINJ1 is reportedly required to induce plasma membrane rupture downstream of GSDMD pore formation. To compare the phenotypes of NINJ1-deficient cells to our results, we generated NINJ1 KOs using Cas9-expressing iBMDMs after electroporation of two independent sgRNAs against NINJ1 (referred to as g1 and g2). After subjecting LPS-primed WT, NINJ1 g1, and NINJ1 g2 iBMDMs to the NLRP3 agonist Nigericin, we observed PI staining that was similar between these genotypes (Figure S6A), but reduction of LDH release in NINJ1-deficient cells (Figure S6B). Similarly, LPS electroporation of LPS-primed NINJ1-deficient cells displayed a marginal reduction in PI staining, but a substantial reduction in LDH release, as compared to WT cells (Figures S6C and S6D). These data position the actions of Ragulator-Rag downstream of GSDMD cleavage and plasma membrane localization, but upstream of NT-GSDMD oligomerization and NINJ1-induced plasma membrane rupture.

DISCUSSION

In this study, a genetic screen was designed to specifically interrogate a single stage in the pyroptosis pathway. This approach was distinct from other genetic screens, where natural upstream stimuli were used (Kayagaki et al., 2015, 2019; Napier et al., 2016; Shi et al., 2015). By focusing on a single (and poorly characterized) stage, we bypassed the possibility of identifying previously defined genes that are necessary for pyroptosis, such as regulators of cell priming or inflammasome assembly. Moreover, our screen employed an internal control (the BFP tag on the GSDMD transgene) to ensure the continued expression of the pore-forming molecule throughout our assays. This quality-control strategy likely explains why we did not identify regulators of transcription and translation in our dataset. Thus, we were able to focus on potential regulators of a process that was considered to be poorly regulated, namely, the steps between cleavage of GSDMD and plasma membrane pore formation. Current models of pyroptosis invoke the process of membrane repair as a negative regulatory mechanism to limit GSDMD activities after this pore-forming factor has been cleaved (Rühl et al., 2018). It was unexpected that we could identify factors that promote GSDMD pore-forming activities post-cleavage, yet our forward genetic screen and subsequent analysis revealed Ragulator-Rag-mTORC1 as factors that act at this stage.

In the metabolic pathways, Ragulator-Rag operates on lysosomes to sense amino acid availability and induce mTOR-dependent cellular responses that depend on mTORC1 (Liu and Sabatini, 2020). Despite its lysosomal localization, mTORC1 has roles in controlling mitochondrial activities (Chen et al., 2008; Cunningham et al., 2007; Schieke et al., 2006). One of these activities appears to be the control of ROS production, which we found is critical for GSDMD oligomerization and pore formation, but not plasma membrane localization of GSDMD. This finding is noteworthy, as biophysical studies have been unable to determine whether GSDMD pores assemble from monomers within the plasma membrane, or whether monomers pre-assemble and then insert an oligomer into the plasma membrane. Our studies suggest the former, as membrane-associated NT-GSDMD monomers can convert into pore-forming oligomers when exposed to ROS inducing agents. However, more work is needed to define these events.

Figure 6. Mitochondrial dysfunction and ROS mediate GSDMD oligomerization

(A) Intracellular ROS levels in live cells of the genotypes indicated by CellRox Deep Red fluorescence after Dox induction (0.5 μg/mL) for 8 h.

(B and C) Western blot of the proteins indicated from combined cell lysates and supernatants under non-reducing (B) or reducing (C) conditions from WT, RagA KO, and RagC KO cells after Dox induction for 8 h and treated with increasing concentrations of H_2O_2 for the last 4 h.

(D) PI uptake by WT, RagA KO, and RagC KO cells after Dox induction for 8 h and treated with 625 μM of H_2O_2 for the last 4 h. MCC950 (10 μM) was added to cells at the start of Dox induction.

(E and F) Western blot of the proteins indicated from combined cell lysates and supernatants under non-reducing (E) or reducing (F) conditions from WT, RagA KO, and RagC KO cells after Dox induction for 8 h and treated with Antimycin A (10 μg/mL), Rotenone (10 μM), or TTFA (100 μM) for the last 4 h.

(G) PI uptake by WT, RagA KO, and RagC KO cells after Dox induction for 8 h and treated with Antimycin A (10 μg/mL), Rotenone (10 μM), or TTFA (100 μM) for the last 4 h.

(H) PI uptake by MCC950-treated cells of the genotypes indicated after Dox induction for 8 h and treated with Antimycin A (10 μg/mL), Rotenone (10 μM), or TTFA (100 μM) for the last 4 h.

(I and J) PI uptake (I) and LDH release into cell-free supernatant (J) from WT iBMDMs treated with FlaTox and indicated concentrations of NAC for 2 h.

(K) Western blot of the proteins indicated from combined cell lysates and supernatants from WT iBMDMs treated with FlaTox and 15 mM NAC for 2 h.

Means and SEM of three (A, D, G, H, and J) or four (I) independent experiments are shown. Two-way ANOVA was used for analysis. See also Figures S5 and S6.

Our results suggest that GSDMD pore-forming activity is dependent on the actions of the mTORC1 component Raptor and the upstream Ragulator-Rag complex. However, this link between GSDMD and Ragulator-Rag-mTORC1 does not require direct interactions between these proteins. Indeed, the ability of ROS to restore GSDMD oligomerization and pore-forming activity in Rag-deficient cells suggests that the principal function of Ragulator-Rag in pyroptosis may be in ROS regulation. If this model is correct, one would expect that other stimuli that promote ROS production would promote GSDMD oligomerization and may even bypass the need for Ragulator-Rag in this process. Additional activators of the mTOR pathway exist, which operate independent of Ragulator-Rag, such as glucose, growth factors, cytokine receptors, and pattern recognition receptors (Liu and Sabatini, 2020). We propose that these types of stimuli may be sufficient to activate mTORC1 and generate ROS that promotes GSDMD oligomerization. Moreover, some inflammasome triggers and microbial infection itself may serve as a source of mTOR activation or ROS production to prime GSDMD for subsequent oligomerization (West et al., 2011). The role of endogenous or microbial activators of these pathways should be investigated in the context of control of GSDMD pore formation in future studies.

A link between metabolism and cell death has been investigated in prior studies, including work demonstrating that NLRP3 and GSDMD can be post-translationally modified by TCA cycle intermediates (Hooftman et al., 2020; Humphries et al., 2020). Moreover, metabolic dysfunction and mitochondrial damage have been investigated in the initiation of death pathway signaling, such as formation of the apoptosome and NLRP3 inflammasomes (Andersen and Kornbluth, 2013; Próchnicki and Latz, 2017). A notable outcome of our study is that our data suggest a metabolic checkpoint exists after activation of the inflammasome and after cleavage of GSDMD. The discovery that upstream regulators of the mTOR pathway define a checkpoint for pore formation and pyroptosis suggests that we can no longer conclude that biochemical assessment of GSDMD cleavage is equivalent to pore formation.

In summary, this study broadens the regulated stages in the pyroptosis pathway to include activities downstream of GSDMD cleavage. These regulatory events are likely specific to activities within cells, as GSDMD has the intrinsic capacity to insert into liposomal membranes upon cleavage by caspase-1 or caspase-11 (Aglietti et al., 2016; Ding et al., 2016; Liu et al., 2016; Sborgi et al., 2016). Based on this idea, it stands to reason that additional cellular factors may exist that control pore formation, pyroptosis, and other innate immune signaling pathways. Our study provides a mandate for "precision screening strategies" to be performed in the innate immune system, where assays for single stages in a pathway may allow for the complexity of cellular activities to be condensed, thereby revealing unexpected regulation of innate immune signal transduction.

Limitations of the study
Our screen identified regulators of GSDMD that operate (post-cleavage) to promote oligomerization and pore formation that leads to pyroptosis. We focused our mechanistic analysis on the Rag GTPases and downstream mTORC1 effectors, but survival enrichment suggests that FLCN and Lamtor1-4 also serve a similar role in promoting mitochondrial ROS and GSDMD pore formation to enforce pyroptosis. In other contexts, RagA and RagB have redundant roles in mTOR activation (Liu and Sabatini, 2020). Thus, other Ragulator-Rag complex members as well as other prominent identified screen hits related to ROS biology, autophagy, or organelle homeostasis should be investigated further. Moreover, our results suggest that the genetic association between the Ragulator-Rag complex and GSDMD may act through downstream effectors of the mTORC1 metabolic pathway, namely, mitochondrial quality control and ROS metabolite production. Mechanistic insights into how mitochondrial ROS may affect GSDMD oligomerization potential await further characterization.

STAR★METHODS

Detailed methods are provided in the online version of this paper and include the following:

- KEY RESOURCES TABLE
- RESOURCE AVAILABILITY
  ○ Lead contact
  ○ Materials availability
  ○ Data availability
- EXPERIMENTAL MODEL AND SUBJECT DETAILS
  ○ Cell culture
- METHOD DETAILS
  ○ Construct preparation
  ○ Primary BMDM generation and immortalization
  ○ Retroviral/Lentiviral transduction
  ○ Chimeric immune editing
  ○ Brie cellular library and screening assay
  ○ Doxycycline induction in engineered cell lines
  ○ Compound treatment
  ○ Neon electroporation
  ○ Characterization of apoptosis
  ○ Bacterial infection
  ○ Confocal microscopy
  ○ Detection of cellular ROS
  ○ Mitochondrial ROS and mitochondrial potential
  ○ Activation assays in HEK293T and HEK293 cells
  ○ Starvation experiment
  ○ Subcellular fractionation
  ○ GSDMD oligomerization assay
  ○ FRAP of CD14 and NT-GSDMD-BFP
  ○ Purification of LFn-Fla from insect cells
  ○ FlaTox stimulation in unprimed phagocytes
  ○ Antibodies and reagents
- QUANTIFICATION AND STATISTICAL ANALYSIS
  ○ Analysis of screening results
  ○ Microscopy image processing
  ○ Statistical analysis

SUPPLEMENTAL INFORMATION

Supplemental information can be found online at https://doi.org/10.1016/j.cell.2021.06.028.

CellPress

AUTHOR CONTRIBUTIONS

DECLARATION OF INTERESTS

REFERENCES

Aglietti, R.A., Estevez, A., Gupta, A., Ramirez, M.G., Liu, P.S., Kayagaki, N., Ciferri, C., Dixit, V.M., and Dueber, E.C. (2016). GsdmD p30 elicited by caspase-11 during pyroptosis forms pores in membranes. Proc. Natl. Acad. Sci. USA *113*, 7858–7863.

Andersen, J.L., and Kornbluth, S. (2013). The tangled circuitry of metabolism and apoptosis. Mol. Cell *49*, 399–410.

Avbelj, M., Wolz, O.O., Fekonja, O., Benčina, M., Repič, M., Mavri, J., Krüger, J., Schärfe, C., Delmiro Garcia, M., Panter, G., et al. (2014). Activation of lymphoma-associated MyD88 mutations via allostery-induced TIR-domain oligomerization. Blood *124*, 3896–3904.

Bauernfeind, F., Bartok, E., Rieger, A., Franchi, L., Núñez, G., and Hornung, V. (2011). Cutting edge: reactive oxygen species inhibitors block priming, but not activation, of the NLRP3 inflammasome. J. Immunol. *187*, 613–617.

Boucher, D., Monteleone, M., Coll, R.C., Chen, K.W., Ross, C.M., Teo, J.L., Gomez, G.A., Holley, C.L., Bierschenk, D., Stacey, K.J., et al. (2018). Caspase-1 self-cleavage is an intrinsic mechanism to terminate inflammasome activity. J. Exp. Med. *215*, 827–840.

Broz, P., Newton, K., Lamkanfi, M., Mariathasan, S., Dixit, V.M., and Monack, D.M. (2010). Redundant roles for inflammasome receptors NLRP3 and NLRC4 in host defense against Salmonella. J. Exp. Med. *207*, 1745–1755.

Chan, A.H., and Schroder, K. (2020). Inflammasome signaling and regulation of interleukin-1 family cytokines. J. Exp. Med. *217*, e20190314.

Chen, C., Liu, Y., Liu, R., Ikenoue, T., Guan, K.L., Liu, Y., and Zheng, P. (2008). TSC-mTOR maintains quiescence and function of hematopoietic stem cells by repressing mitochondrial biogenesis and reactive oxygen species. J. Exp. Med. *205*, 2397–2408.

Chen, K.W., Groß, C.J., Sotomayor, F.V., Stacey, K.J., Tschopp, J., Sweet, M.J., and Schroder, K. (2014). The neutrophil NLRC4 inflammasome selectively promotes IL-1β maturation without pyroptosis during acute Salmonella challenge. Cell Rep. *8*, 570–582.

Coll, R.C., Hill, J.R., Day, C.J., Zamoshnikova, A., Boucher, D., Massey, N.L., Chitty, J.L., Fraser, J.A., Jennings, M.P., Robertson, A.A.B., and Schroder, K. (2019). MCC950 directly targets the NLRP3 ATP-hydrolysis motif for inflammasome inhibition. Nat. Chem. Biol. *15*, 556–559.

Condon, K.J., Orozco, J.M., Adelmann, C.H., Spinelli, J.B., van der Helm, P.W., Roberts, J.M., Kunchok, T., and Sabatini, D.M. (2021). Genome-wide CRISPR screens reveal multitiered mechanisms through which mTORC1 senses mitochondrial dysfunction. Proc. Natl. Acad. Sci. USA *118*, e2022120118.

Cunningham, J.T., Rodgers, J.T., Arlow, D.H., Vazquez, F., Mootha, V.K., and Puigserver, P. (2007). mTOR controls mitochondrial oxidative function through a YY1-PGC-1alpha transcriptional complex. Nature *450*, 736–740.

de Vasconcelos, N.M., Van Opdenbosch, N., Van Gorp, H., Parthoens, E., and Lamkanfi, M. (2019). Single-cell analysis of pyroptosis dynamics reveals conserved GSDMD-mediated subcellular events that precede plasma membrane rupture. Cell Death Differ. *26*, 146–161.

Dinarello, C.A. (2018). Overview of the IL-1 family in innate inflammation and acquired immunity. Immunol. Rev. *281*, 8–27.

Ding, J., Wang, K., Liu, W., She, Y., Sun, Q., Shi, J., Sun, H., Wang, D.C., and Shao, F. (2016). Pore-forming activity and structural autoinhibition of the gasdermin family. Nature *535*, 111–116.

Doench, J.G., Fusi, N., Sullender, M., Hegde, M., Vaimberg, E.W., Donovan, K.F., Smith, I., Tothova, Z., Wilen, C., Orchard, R., et al. (2016). Optimized sgRNA design to maximize activity and minimize off-target effects of CRISPR-Cas9. Nat. Biotechnol. *34*, 184–191.

Dostert, C., Pétrilli, V., Van Bruggen, R., Steele, C., Mossman, B.T., and Tschopp, J. (2008). Innate immune activation through Nalp3 inflammasome sensing of asbestos and silica. Science *320*, 674–677.

Evavold, C.L., Ruan, J., Tan, Y., Xia, S., Wu, H., and Kagan, J.C. (2018). The Pore-Forming Protein Gasdermin D Regulates Interleukin-1 Secretion from Living Macrophages. Immunity *48*, 35–44.

Franchi, L., Amer, A., Body-Malapel, M., Kanneganti, T.D., Ozören, N., Jagirdar, R., Inohara, N., Vandenabeele, P., Bertin, J., Coyle, A., et al. (2006). Cytosolic flagellin requires Ipaf for activation of caspase-1 and interleukin 1beta in salmonella-infected macrophages. Nat. Immunol. *7*, 576–582.

Hagar, J.A., Powell, D.A., Aachoui, Y., Ernst, R.K., and Miao, E.A. (2013). Cytoplasmic LPS activates caspase-11: implications in TLR4-independent endotoxic shock. Science *341*, 1250–1253.

Haggie, P.M., and Verkman, A.S. (2008). Monomeric CFTR in plasma membranes in live cells revealed by single molecule fluorescence imaging. J. Biol. Chem. *283*, 23510–23513.

Heilig, R., Dick, M.S., Sborgi, L., Meunier, E., Hiller, S., and Broz, P. (2018). The Gasdermin-D pore acts as a conduit for IL-1β secretion in mice. Eur. J. Immunol. *48*, 584–592.

Hooftman, A., Angiari, S., Hester, S., Corcoran, S.E., Runtsch, M.C., Ling, C., Ruzek, M.C., Slivka, P.F., McGettrick, A.F., Banahan, K., et al. (2020). The Immunomodulatory Metabolite Itaconate Modifies NLRP3 and Inhibits Inflammasome Activation. Cell Metab. *32*, 468–478.

Howell, J.J., and Manning, B.D. (2011). mTOR couples cellular nutrient sensing to organismal metabolic homeostasis. Trends Endocrinol. Metab. *22*, 94–102.

Hu, J., Zacharek, S., He, Y.J., Lee, H., Shumway, S., Duronio, R.J., and Xiong, Y. (2008). WD40 protein FBW5 promotes ubiquitination of tumor suppressor TSC2 by DDB1-CUL4-ROC1 ligase. Genes Dev. *22*, 866–871.

Hu, J.J., Liu, X., Xia, S., Zhang, Z., Zhang, Y., Zhao, J., Ruan, J., Luo, X., Lou, X., Bai, Y., et al. (2020). FDA-approved disulfiram inhibits pyroptosis by blocking gasdermin D pore formation. Nat. Immunol. 21, 736–745.

Humphries, F., Shmuel-Galia, L., Ketelut-Carneiro, N., Li, S., Wang, B., Nemmara, V.V., Wilson, R., Jiang, Z., Khalighinejad, F., Muneeruddin, K., et al. (2020). Succination inactivates gasdermin D and blocks pyroptosis. Science 369, 1633–1637.

Jia, J., Abudu, Y.P., Claude-Taupin, A., Gu, Y., Kumar, S., Choi, S.W., Peters, R., Mudd, M.H., Allers, L., Salemi, M., et al. (2018). Galectins Control mTOR in Response to Endomembrane Damage. Mol. Cell 70, 120–135.

Kayagaki, N., Wong, M.T., Stowe, I.B., Ramani, S.R., Gonzalez, L.C., Akashi-Takamura, S., Miyake, K., Zhang, J., Lee, W.P., Muszyński, A., et al. (2013). Noncanonical inflammasome activation by intracellular LPS independent of TLR4. Science 341, 1246–1249.

Kayagaki, N., Stowe, I.B., Lee, B.L., O'Rourke, K., Anderson, K., Warming, S., Cuellar, T., Haley, B., Roose-Girma, M., Phung, Q.T., et al. (2015). Caspase-11 cleaves gasdermin D for non-canonical inflammasome signalling. Nature 526, 666–671.

Kayagaki, N., Lee, B.L., Stowe, I.B., Kornfeld, O.S., O'Rourke, K., Mirrashidi, K.M., Haley, B., Watanabe, C., Roose-Girma, M., Modrusan, Z., et al. (2019). IRF2 transcriptionally induces GSDMD expression for pyroptosis. Sci. Signal. 12, eaax4917.

Kayagaki, N., Kornfeld, O.S., Lee, B.L., Stowe, I.B., O'Rourke, K., Li, Q., Sandoval, W., Yan, D., Kang, J., Xu, M., et al. (2021). NINJ1 mediates plasma membrane rupture during lytic cell death. Nature 591, 131–136.

Kofoed, E.M., and Vance, R.E. (2011). Innate immune recognition of bacterial ligands by NAIPs determines inflammasome specificity. Nature 477, 592–595.

Kovacs, S.B., and Miao, E.A. (2017). Gasdermins: Effectors of Pyroptosis. Trends Cell Biol. 27, 673–684.

LaFleur, M.W., Nguyen, T.H., Coxe, M.A., Yates, K.B., Trombley, J.D., Weiss, S.A., Brown, F.D., Gillis, J.E., Coxe, D.J., Doench, J.G., et al. (2019). A CRISPR-Cas9 delivery system for in vivo screening of genes in the immune system. Nat. Commun. 10, 1668.

Li, J., Yin, H.L., and Yuan, J. (2008). Flightless-I regulates proinflammatory caspases by selectively modulating intracellular localization and caspase activity. J. Cell Biol. 181, 321–333.

Lieberman, J., Wu, H., and Kagan, J.C. (2019). Gasdermin D activity in inflammation and host defense. Sci. Immunol. 4, eaav1447.

Liu, G.Y., and Sabatini, D.M. (2020). mTOR at the nexus of nutrition, growth, ageing and disease. Nat. Rev. Mol. Cell Biol. 21, 183–203.

Liu, X., Zhang, Z., Ruan, J., Pan, Y., Magupalli, V.G., Wu, H., and Lieberman, J. (2016). Inflammasome-activated gasdermin D causes pyroptosis by forming membrane pores. Nature 535, 153–158.

Liu, Z., Wang, C., Yang, J., Zhou, B., Yang, R., Ramachandran, R., Abbott, D.W., and Xiao, T.S. (2019). Crystal Structures of the Full-Length Murine and Human Gasdermin D Reveal Mechanisms of Autoinhibition, Lipid Binding, and Oligomerization. Immunity 51, 43–49.

Man, S.M., Hopkins, L.J., Nugent, E., Cox, S., Glück, I.M., Tourlomousis, P., Wright, J.A., Cicuta, P., Monie, T.P., and Bryant, C.E. (2014). Inflammasome activation causes dual recruitment of NLRC4 and NLRP3 to the same macromolecular complex. Proc. Natl. Acad. Sci. USA 111, 7403–7408.

Moon, J.S., Hisata, S., Park, M.A., DeNicola, G.M., Ryter, S.W., Nakahira, K., and Choi, A.M.K. (2015). mTORC1-Induced HK1-Dependent Glycolysis Regulates NLRP3 Inflammasome Activation. Cell Rep. 12, 102–115.

Napier, B.A., Brubaker, S.W., Sweeney, T.E., Monette, P., Rothmeier, G.H., Gertsvolf, N.A., Puschnik, A., Carette, J.E., Khatri, P., and Monack, D.M. (2016). Complement pathway amplifies caspase-11-dependent cell death and endotoxin-induced sepsis severity. J. Exp. Med. 213, 2365–2382.

Orning, P., Weng, D., Starheim, K., Ratner, D., Best, Z., Lee, B., Brooks, A., Xia, S., Wu, H., Kelliher, M.A., et al. (2018). Pathogen blockade of TAK1 triggers caspase-8-dependent cleavage of gasdermin D and cell death. Science 362, 1064–1069.

Platt, R.J., Chen, S., Zhou, Y., Yim, M.J., Swiech, L., Kempton, H.R., Dahlman, J.E., Parnas, O., Eisenhaure, T.M., Jovanovic, M., et al. (2014). CRISPR-Cas9 knockin mice for genome editing and cancer modeling. Cell 159, 440–455.

Próchnicki, T., and Latz, E. (2017). Inflammasomes on the Crossroads of Innate Immune Recognition and Metabolic Control. Cell Metab. 26, 71–93.

Rathinam, V.A., Vanaja, S.K., Waggoner, L., Sokolovska, A., Becker, C., Stuart, L.M., Leong, J.M., and Fitzgerald, K.A. (2012). TRIF licenses caspase-11-dependent NLRP3 inflammasome activation by gram-negative bacteria. Cell 150, 606–619.

Rauch, I., Tenthorey, J.L., Nichols, R.D., Al Moussawi, K., Kang, J.J., Kang, C., Kazmierczak, B.I., and Vance, R.E. (2016). NAIP proteins are required for cytosolic detection of specific bacterial ligands in vivo. J. Exp. Med. 213, 657–665.

Rauch, I., Deets, K.A., Ji, D.X., von Moltke, J., Tenthorey, J.L., Lee, A.Y., Philip, N.H., Ayres, J.S., Brodsky, I.E., Gronert, K., and Vance, R.E. (2017). NAIP-NLRC4 Inflammasomes Coordinate Intestinal Epithelial Cell Expulsion with Eicosanoid and IL-18 Release via Activation of Caspase-1 and -8. Immunity 46, 649–659.

Rogala, K.B., Gu, X., Kedir, J.F., Abu-Remaileh, M., Bianchi, L.F., Bottino, A.M.S., Dueholm, R., Niehaus, A., Overwijn, D., Fils, A.P., et al. (2019). Structural basis for the docking of mTORC1 on the lysosomal surface. Science 366, 468–475.

Ruan, J., Xia, S., Liu, X., Lieberman, J., and Wu, H. (2018). Cryo-EM structure of the gasdermin A3 membrane pore. Nature 557, 62–67.

Rühl, S., Shkarina, K., Demarco, B., Heilig, R., Santos, J.C., and Broz, P. (2018). ESCRT-dependent membrane repair negatively regulates pyroptosis downstream of GSDMD activation. Science 362, 956–960.

Sancak, Y., Bar-Peled, L., Zoncu, R., Markhard, A.L., Nada, S., and Sabatini, D.M. (2010). Ragulator-Rag complex targets mTORC1 to the lysosomal surface and is necessary for its activation by amino acids. Cell 141, 290–303.

Sarhan, J., Liu, B.C., Muendlein, H.I., Li, P., Nilson, R., Tang, A.Y., Rongvaux, A., Bunnell, S.C., Shao, F., Green, D.R., et al. (2018). Caspase-8 induces cleavage of gasdermin D to elicit pyroptosis during Yersinia infection. PNAS 115, E10888–E10897.

Sborgi, L., Rühl, S., Mulvihill, E., Pipercevic, J., Heilig, R., Stahlberg, H., Farady, C.J., Müller, D.J., Broz, P., and Hiller, S. (2016). GSDMD membrane pore formation constitutes the mechanism of pyroptotic cell death. EMBO J. 35, 1766–1778.

Schieke, S.M., Phillips, D., McCoy, J.P., Jr., Aponte, A.M., Shen, R.F., Balaban, R.S., and Finkel, T. (2006). The mammalian target of rapamycin (mTOR) pathway regulates mitochondrial oxygen consumption and oxidative capacity. J. Biol. Chem. 281, 27643–27652.

Shen, K., Rogala, K.B., Chou, H.T., Huang, R.K., Yu, Z., and Sabatini, D.M. (2019). Cryo-EM Structure of the Human FLCN-FNIP2-Rag-Ragulator Complex. Cell 179, 1319–1329.

Shi, J., Zhao, Y., Wang, Y., Gao, W., Ding, J., Li, P., Hu, L., and Shao, F. (2014). Inflammatory caspases are innate immune receptors for intracellular LPS. Nature 514, 187–192.

Shi, J., Zhao, Y., Wang, K., Shi, X., Wang, Y., Huang, H., Zhuang, Y., Cai, T., Wang, F., and Shao, F. (2015). Cleavage of GSDMD by inflammatory caspases determines pyroptotic cell death. Nature 526, 660–665.

Shimada, K., Crother, T.R., Karlin, J., Dagvadorj, J., Chiba, N., Chen, S., Ramanujan, V.K., Wolf, A.J., Vergnes, L., Ojcius, D.M., et al. (2012). Oxidized mitochondrial DNA activates the NLRP3 inflammasome during apoptosis. Immunity 36, 401–414.

Stewart, S.A., Dykxhoorn, D.M., Palliser, D., Mizuno, H., Yu, E.Y., An, D.S., Sabatini, D.M., Chen, I.S., Hahn, W.C., Sharp, P.A., et al. (2003). Lentivirus-delivered stable gene silencing by RNAi in primary cells. RNA 9, 493–501.

Tapia-Abellán, A., Angosto-Bazarra, D., Martínez-Banaclocha, H., de Torre-Minguela, C., Cerón-Carrasco, J.P., Pérez-Sánchez, H., Arostegui, J.I., and Pelegrin, P. (2019). MCC950 closes the active conformation of NLRP3 to an inactive state. Nat. Chem. Biol. 15, 560–564.

Thoreen, C.C., Kang, S.A., Chang, J.W., Liu, Q., Zhang, J., Gao, Y., Reichling, L.J., Sim, T., Sabatini, D.M., and Gray, N.S. (2009). An ATP-competitive

mammalian target of rapamycin inhibitor reveals rapamycin-resistant functions of mTORC1. J. Biol. Chem. *284*, 8023–8032.

von Moltke, J., Trinidad, N.J., Moayeri, M., Kintzer, A.F., Wang, S.B., van Rooijen, N., Brown, C.R., Krantz, B.A., Leppla, S.H., Gronert, K., and Vance, R.E. (2012). Rapid induction of inflammatory lipid mediators by the inflammasome in vivo. Nature *490*, 107–111.

Wang, K., Sun, Q., Zhong, X., Zeng, M., Zeng, H., Shi, X., Li, Z., Wang, Y., Zhao, Q., Shao, F., and Ding, J. (2020). Structural Mechanism for GSDMD Targeting by Autoprocessed Caspases in Pyroptosis. Cell *180*, 941–955.

West, A.P., Brodsky, I.E., Rahner, C., Woo, D.K., Erdjument-Bromage, H., Tempst, P., Walsh, M.C., Choi, Y., Shadel, G.S., and Ghosh, S. (2011). TLR signalling augments macrophage bactericidal activity through mitochondrial ROS. Nature *472*, 476–480.

Wilkinson, A.C., Ishida, R., Kikuchi, M., Sudo, K., Morita, M., Crisostomo, R.V., Yamamoto, R., Loh, K.M., Nakamura, Y., Watanabe, M., et al. (2019). Long-term ex vivo haematopoietic-stem-cell expansion allows nonconditioned transplantation. Nature *571*, 117–121.

Yang, H., Yu, Z., Chen, X., Li, J., Li, N., Cheng, J., Gao, N., Yuan, H.X., Ye, D., Guan, K.L., and Xu, Y. (2021). Structural insights into TSC complex assembly and GAP activity on Rheb. Nat. Commun. *12*, 339.

Zhao, Y., Yang, J., Shi, J., Gong, Y.N., Lu, Q., Xu, H., Liu, L., and Shao, F. (2011). The NLRC4 inflammasome receptors for bacterial flagellin and type III secretion apparatus. Nature *477*, 596–600.

Zhou, R., Yazdi, A.S., Menu, P., and Tschopp, J. (2011). A role for mitochondria in NLRP3 inflammasome activation. Nature *469*, 221–225.

STAR★METHODS

KEY RESOURCES TABLE

REAGENT or RESOURCE	SOURCE	IDENTIFIER
Antibodies		
Armenian Hamster monoclonal to CD3ε (PE)	Biolegend	Clone 145-2C11; 100308; RRID: AB_312673
Goat Anti-Rabbit IgG H&L (HRP)	Abcam	ab6721; RRID:AB_955447
Mouse monoclonal Anti- *S. pyogenes* Cas9	Abcam	ab191468; RRID:AB_2692325
Mouse monoclonal Anti-TetR	Takara	631131
Mouse monoclonal Anti-β actin	Sigma-Aldrich	A5441; RRID:AB_476744
Mouse monoclonal Anti-β actin	Cell Signaling Technology	3700S; RRID:AB_2242334
Mouse monoclonal to tubulin (beta)	Developmental Studies Hybridoma Bank	Clone E7 RRID: AB_2315513
Peroxidase AffiniPure Goat Anti-Mouse IgG (H+L)	Jackson ImmunoResearch	115-035-003; RRID:AB_10015289
Peroxidase AffiniPure Goat Anti-Rabbit IgG (H+L)	Jackson ImmunoResearch	111-035-003; RRID:AB_2313567
Peroxidase AffiniPure Goat Anti-Rat IgG (H+L)	Jackson ImmunoResearch	112-035-003; RRID:AB_2338128
Rabbit monoclonal [EPR19829] to GSDMD	Abcam	ab210070
Rabbit monoclonal [EPR20829-408] to cleaved N-terminal human GSDMD	Abcam	ab215203
Rabbit monoclonal Anti- phospho-p70 S6 kinase (Thr389)	Cell Signaling Technology	9234S; RRID:AB_2269803
Rabbit monoclonal Anti- *S. pyogenes* Cas9	Cell Signaling Technologies	65832S; RRID:AB_2799695
Rabbit monoclonal Anti-RagA	Cell Signaling Technology	4357S; RRID:AB_10545136
Rabbit monoclonal Anti-RagC	Cell Signaling Technology	5466S; RRID:AB_10692651
Rabbit monoclonal Anti-Raptor	Cell Signaling Technology	2280S; RRID:AB_561245
Rabbit monoclonal Anti-Rictor	Cell Signaling Technology	2114S; RRID:AB_2179963
Rabbit monoclonal p70 S6 kinase (49D7)	Cell Signaling Technology	2708S; RRID:AB_390722
Rabbit polyclonal Anti-tagRFP	Evrogen	AB233; RRID:AB_2571743
Rabbit polyclonal Anti-β actin	Cell Signaling Technology	#4967; RRID:AB_330288
Rabbit polyclonal to Na/K ATPase	Cell Signaling Technology	3010S; RRID: AB_2060983
Rabbit polyclonal to pro-IL-1β	GeneTex	GTX74034; RRID: AB_378141
Rat monoclonal to B220 (PE)	Biolegend	Clone RA3-6B2; 103208; RRID: AB_312993
Rat monoclonal to CD5 (PE)	Biolegend	Clone 53-7.3; 100608; RRID: AB_312737
Rat monoclonal to CD11b (APC)	ThermoFisher Scientific	Clone M1/70; 17-0112-82; RRID: AB_469343
Rat monoclonal to CD11b (PE)	Biolegend	Clone M1/70; 101208; RRID: AB_312791
Rat monoclonal to CD117 (APC)	Biolegend	Clone ACK2; 135108; RRID: AB_2028407
Rat monoclonal to CD14 (PE)	ThermoFisher Scientific	Clone Sa2-8; 12-0141-82; RRID: AB_465563
Rat monoclonal to Gr-1 (PE)	Biolegend	Clone RB6-8C5; 108408; RRID: AB_313373
Rat monoclonal to Sca-1 (BV421)	Biolegend	Clone D7; 108128; RRID: AB_2563064
Rat monoclonal to TER-119 (PE)	Biolegend	Clone TER-119; 116208; RRID: AB_313709
TruStain FcX	Biolegend	101320; RRID: AB_1574975
Bacterial and virus strains		
Brie sgRNA lentiviral particles with Basticidin resistance	Broad Institute	N/A
Escherichia coli Stbl3	Invitrogen	C737303

(Continued on next page)

Continued

REAGENT or RESOURCE	SOURCE	IDENTIFIER
Escherichia coli TOP10	Invitrogen	C404010
Salmonella enterica serovar Typhimurium (SL1344)	Denise Monack Lab	N/A
Chemicals, peptides, and recombinant proteins		
Antimycin A from Streptomyces sp.	Sigma	A8674-50MG
BamHI restriction enzyme	ThermoFisher Scientific	ER0055
Benzamidine	Sigma Aldrich	B6506
Blasticidin	ThermoFisher Scientific	A1113903
BsmbI restriction enzyme	NEB	R0580L
CellROX Deep Red Reagent	Invitrogen	C10422
Cholera toxin subunit B Alexa fluor 647	Invitrogen	C34778
Complete protease inhibitor tablets	Sigma Aldrich	11836170001
Dimethyl sulfoxide	Sigma Aldrich	D2438
Disulfiram	Sigma Aldrich	86720
Doxycycline hyclate	Sigma Aldrich	D9891-1G
Dulbecco's MEM, high glucose, L-glut, pyruvate	ThermoFisher Scientific	11995-073
Dulbecco's MEM w/o Amino Acids and glucose	USBiological	D9800-27
E. coli LPS Serotype O111:B4 S-form	Enzo Life Sciences	ALX-581-012-L002
EcoRI restriction enzyme	ThermoFisher Scientific	ER0275
Fetal bovine serum	ThermoFisher Scientific/GIBCO	10500064
G418	Invivogen	ant-gn-5
Glucose Solution	ThermoFisher Scientific	A2494001
Ham's F12	VWR	12001-578
HEPES	VWR	97064-360
Hydrogen peroxide (30% w/w) stock solution	Sigma	H1009-100ML
InstantBlue stain	Expedeon	ISB1L
ITSX	ThermoFisher Scientific	51500056
L-glutamine	ThermoFisher Scientific	25030081; 25030164
Lipofectamine 2000	Invitrogen	11668019
MCC950	Avistron	AV02509
MCC950	Invivogen	inh-mcc
MEM Amino Acids Solution (50X)	ThermoFisher Scientific	11130036
MEM Non-essential Amino Acids Solution	ThermoFisher Scientific	11140035
MHY1485	Calbiochem	5005540001
MitoSOX	Invitrogen/Molecular probes	M36008
MitoTracker Deep Red FM	Invitrogen	M22426
N-acetyl cysteine	Sigma	A9165-25G
Nigericin	Sigma Aldrich	N7143
Nigericin	Invivogen	tlrl-nig-5
OptiMEM reduced serum media	ThermoFisher Scientific	31985062
PEI	Polysciences	24765-2
Pen/Strep	ThermoFisher Scientific	15-140-122; 15-140-163
Phusion HF Polymerase	ThermoFisher Scientific	F-530L
PMSF	Sigma Aldrich	10837091001
Polybrene	MerckMillipore	TR-1003-G
Propidium iodide	Sigma	P4864-10ML
Protective Antigen	List Biological Labs	#171E

Continued

REAGENT or RESOURCE	SOURCE	IDENTIFIER
Puromycin	Invivogen	ant-pr-1
PVA (Poly-vinyl alcohol)	Sigma Aldrich	P8136
Rapamycin	Sigma Aldrich	R0395
Retronectin	Takara	T100B
Rotenone	Tocris	3616
SCF (Recombinant mouse stem cell factor)	Peprotech	AF-250-03
SFX-insect media	GE Healthcare	SH30278
Sodium Pyruvate	ThermoFisher Scientific	11360070
Staurosporine	Tocris	1285
Sulfamethoxazole-Trimethoprim	Patterson Veterinary	07-893-6107
TMRM	Invitrogen	T668
Torin-1	Santa cruz biotechnology	sc-396760
TPO (Recombinant mouse Thrombopoietin)	Peprotech	AF-315-14
TTFA (2-Thenoyltrifluoroacetone)	Sigma	T27006-25G
Critical commercial assays		
100 μl Tip Neon Transfection Kit	ThermoFisher Scientific	MPK10096
CD117 Microbeads, mouse	Miltenyi Biotec	130-091-224
CyQuant LDH Cytotoxicity Assay Kit	ThermoFisher Scientific	C20301
Mouse IL-1β ELISA Kit	ThermoFisher Scientific	88-7013-86
NucleoSpin Blook XL	Clontech	740950.5
OneStep PCR Inhibitor Removal Kit	Zymo Research	D6030
Pacific Blue Annexin V Apoptosis Detection Kit with 7-AAD	Biolegend	640926
Experimental models: Cell lines		
Ampho-Gryphon retroviral packaging cell line	Allelle Biotech	ABP-RVK-10001
Control HEK293T	David Sabatini Rogala et al., 2019	N/A
CREJ2 (cells producing J2 retroviral particles)	Jonathan Kagan Laboratory	N/A
HEK293T	Jonathan Kagan Laboratory	N/A
HEK293	ATTC	CRL-1573
iBMDM C57BL/6J (WT)	This paper	N/A
iBMDM Cas9 KI NINJ1 g1	This paper	N/A
iBMDM Cas9 KI NINJ1 g2	This paper	N/A
iBMDM Cas9 KI Tet3G Doxycycline Inducible FL-GSDMD-BFP	This paper	N/A
iBMDM Cas9 KI Tet3G Doxycycline Inducible NT-GSDMD-BFP	This paper	N/A
iBMDM Cas9 KI Tet3G Doxycycline Inducible NT-GSDMD-BFP pXPR-054-empty vector	This paper	N/A
iBMDM Cas9 KI Tet3G Doxycycline Inducible NT-GSDMD-BFP pXPR-054-RagC-sgRNA1	This paper	N/A
iBMDM Cas9 KI Tet3G Doxycycline Inducible NT-GSDMD-BFP pXPR-054-RagC-sgRNA2	This paper	N/A
iBMDM Cas9 KI Tet3G Doxycycline Inducible NT-GSDMD-BFP pXPR-054-RagA-sgRNA1	This paper	N/A

Continued

REAGENT or RESOURCE	SOURCE	IDENTIFIER
iBMDM Cas9 KI Tet3G Doxycycline Inducible NT-GSDMD-BFP pXPR-054-RagA-sgRNA2	This paper	N/A
iBMDM Cas9 KI Tet3G stable	This paper	N/A
iBMDM Cas9 Knock In (KI)	This paper	N/A
iBMDM GSDMD deficient	This paper	N/A
iBMDM LysM CRE (LysM-CRE WT)	This paper	N/A
iBMDM LysM CRE x Raptor flox/flox (LysM-CRE Raptor deficient)	This paper	N/A
iBMDM LysM CRE x Rictor flox/flox (LysM-CRE Rictor deficient)	This paper	N/A
iBMDM NLRP3 deficient	This paper	N/A
Platinum-GP retroviral packaging cell line	Cell Biolabs	RV-103
RagA/B-DKO HEK293T	David Sabatini Rogala et al., 2019	N/A
Sf9 insect cells	Hao Wu	N/A
Experimental models: Organisms/strains		
C57BL6/J WT	Arlene Sharpe Lab	Jax: 000664
Rosa26-LSL-Cas9 knockin on B6J	Arlene Sharpe Lab	Jax: 026175
Zp3-Cre	Arlene Sharpe Lab	Jax: 003651
Oligonucleotides		
I105N-F: GGAGAAGGGAAAAATTCTG GTGGGGCT	This paper, IDT	N/A
I105N-R: AGCCCCACCAGAATTTTTC CCTTCTCC	This paper, IDT	N/A
BamHI-GSDMD CGGATCCGCCACC ATGCCATCGGCCTTTGAGAAAG	This paper, IDT	N/A
R-BFPlink-GSDMDfl CTCATCCC CCCTGATCCTCCACAAGGTTTC TGGCCTAGACTTGA	This paper, IDT	N/A
F-GSDMDFL-link-BFP CCTTGTGGAG GATCAGGGGGGATGAGCGAGCTGA TTAAGGAGAAC	This paper, IDT	N/A
R-BFP-link-GSDMDNt CTCATCCCCC CCTGATCCTCCATCTGACAGGAGA CTGAGCTG	This paper, IDT	N/A
F-GSDMDNt-Link-BFP TCAGATGGA GGATCAGGGGGGATGAGCGAGCT GATTAAGGAGAAC	This paper, IDT	N/A
R-BFP GGAATTCCTTAATTAAGCTT GTGCCCCAGTTTG	This paper, IDT	N/A
Rragc_F1: CACCGCTTCCAGGACGACT ACATGG	This paper, IDT	N/A
Rragc_R1: AAACCCATGTAGTCGTCCT GGAAGC	This paper, IDT	N/A
Rragc_F2: CACCGTTTCTGTACCACCT TACTGA	This paper, IDT	N/A
Rragc_R2: AAACTCAGTAAGGTGGTAC AGAAAC	This paper, IDT	N/A
Rraga_F1: CACCGGGTTCCCCAAGAAT CGGACG	This paper, IDT	N/A
Rraga_R1: AAACCGTCCGATTCTTGGG GAACCC	This paper, IDT	N/A

(Continued on next page)

Continued

REAGENT or RESOURCE	SOURCE	IDENTIFIER
Rraga_F2: CACCGGATCAGCTGATAGACGATGC	This paper, IDT	N/A
Rraga_R2: AAACGCATCGTCTATCAGCTGATCC	This paper, IDT	N/A
I104N-F: CAGGACAGGCAAAGAACGCAGGCGGGGC	This paper, IDT	N/A
I104N-R: GCCCCGCCTGCGTTCTTTGCCTGTCCTG	This paper, IDT	N/A
L290D-F: GACTTCCAGGGCGACCGGGCAGAGGTG	This paper, IDT	N/A
L290D-R: CACCTCTGCCCGGTCGCCCTGGAAGTC	This paper, IDT	N/A
NotI dDmrB-F: TTGCGGCCGCGCCACCATGGGCGTCCAAGTCGAAA	This paper, IDT	N/A
link DmrB-R: GACCCCCCTGATCCTCCTTCCAGTTTTAGAAGCTCCACATCG	This paper, IDT	N/A
link Casp1 ΔCARD -F: AAGGAGGATCAGGGGGGTCAGCTCCATCAGCTGAAACAT	This paper, IDT	N/A
XbaI Casp1-R: GCTCTAGACTATGGTACCGGATCCCCCG	This paper, IDT	N/A
NINJ1 exon 2 genomic locus Fwd: TGTGTGCAGAGGTTGGTGTT	This paper, IDT	N/A
NINJ1 exon 2 genomic locus Rev: AGTCACAGCTTGGGCCATAC	This paper, IDT	N/A
NINJ1 complete synthetic sgRNA (g1): TGCCAACAAGAAGAGCGCTG	IDT	Mm.Cas9.NINJ1.1.AA
NINJ1 complete synthetic sgRNA (g2): GACCACAAGGGGCACGAAGA	IDT	Mm.Cas9.NINJ1.1.AG
Recombinant DNA		
Casp1-flag	Addgene; Junying Yuan Li et al., 2008	Plasmid #21142; RRID: Addgene_21142
GSDMD cDNA ORF Clone in Cloning Vector, Mouse	Sino Biological	MG5A2835-U
pcDNA3 dDMRB-casp1ΔCARD	This paper	N/A
pcDNA3 hFL-GSDMD	This paper	N/A
pcDNA3 hFL-GSDMD (L290D)	This paper	N/A
pcDNA3 hNT-GSDMD	This paper	N/A
pcDNA3 hNT-GSDMD (I104N)	This paper	N/A
pcDNA3 MyD88 L265P	Roman Jerala Avbelj et al., 2014	N/A
pcDNA3-HA3-TSC1	Addgene; Yue Xiong Hu et al., 2008	Plasmid #19911; RRID: Addgene_19911
pCMV-VSV-G	Addgene; Bob Weinberg Stewart et al., 2003	Plasmid #8454; RRID: Addgene_8454
pELAM1-luciferase (NF-κB promotor)	Carsten Kirschning	N/A
pFastBacDual with LFn-Fla	Addgene; Russell Vance Rauch et al., 2016	Plasmid #84866; RRID: Addgene_84866
pHom-Mem1	Clontech	635064
phRL-TK Renilla	Promega	GenBank: AF025846.2
pMD2.g	Addgene; Didier Trono	Plasmid #12259; RRID: Addgene_12259
pRETROX Tre3G/GSDMD-FL-tagBFP	This paper	N/A
pRetroX-Tet3G	Clontech	631188
pRETROX-Tre3G	Clontech	631188

(*Continued on next page*)

Continued

REAGENT or RESOURCE	SOURCE	IDENTIFIER
pRETROX-Tre3G/GSDMD(I105N)-Nt-tagBFP	This paper	N/A
psPAX2	Addgene; Didier Trono	Plasmid #12260; RRID: Addgene_12260
pTagBFP-N	Evrogen	FP172
pXPR-053	Addgene; Arlene Sharpe LaFleur et al., 2019	Plasmid #113591; RRID: Addgene_113591
pXPR-053-RagA-sgRNA1	This paper	N/A
pXPR-053-RagA-sgRNA2	This paper	N/A
pXPR-053-untargeted-control-sgRNA	Arlene Sharpe LaFleur et al., 2019	N/A
pXPR-054 sgRNA expression vector with Blasticidin resistance	Broad Institute GPP	N/A
pXPR-054-RagA-sgRNA1	This paper	N/A
pXPR-054-RagA-sgRNA2	This paper	N/A
pXPR-054-RagC-sgRNA1	This paper	N/A
pXPR-054-RagC-sgRNA2	This paper	N/A
Software and algorithms		
Broad GPP analysis tool	https://portals.broadinstitute.org/gpp/public/	N/A
Fiji / ImageJ version 2.0.0	https://imagej.net/software/fiji	N/A
FlowJo (v10.3.0)	FlowJo	N/A
GOrilla GO analysis tool	http://cbl-gorilla.cs.technion.ac.il/	N/A
GraphPad Prism 8.0	GraphPad Software	N/A
Microsoft Excel	Microsoft	N/A
Microsoft Powerpoint	Microsoft	N/A
Synthego ICE analysis tool	https://ice.synthego.com/#/	N/A
Other		
Costar, Black 96 well plate w/ lid, clear flat bottom, TC treated	Costar	3603
HiTrap Q HP 1 ml column	GE Healthcare	17115301
Live cell imaging, μ-Dish 35 mm, high	Ibidi	81156
μ-slide 8 well	Ibidi	80826
Ni-NTA agarose beads	QIAGEN	30230
PD-10 Desalting columns	GE Healthcare	17085101

RESOURCE AVAILABILITY

Lead contact
Further information and requests for resources and reagents should be directed to and will be fulfilled by the lead contact, Jonathan C. Kagan (jonathan.kagan@childrens.harvard.edu).

Materials availability
All materials generated in this study are available from the lead contact.

Data availability
De-multiplexed FASTQ files and corresponding raw read counts for uninduced input and sorted BFP+ samples have been deposited at the Sequence Read Archive (SRA) and are publicly available as of the date of publication. PRJNA742124 is the BioProject number associated with data from this manuscript. GEO accession number: GSE179089. SRA number: SRP325926.

EXPERIMENTAL MODEL AND SUBJECT DETAILS

Cell culture
Immortalized macrophages, HEK293, HEK293T cell lines were cultured in complete DMEM with 10% FBS (GIBCO) and Penicillin Streptomycin (GIBCO) with added supplements of L-glutamine (GIBCO) and sodium pyruvate (GIBCO) at 37°C and 5% CO_2.

METHOD DETAILS

Construct preparation

For inducible expression upon retroviral transduction, all constructs were inserted into pRETROX Tre3G plasmid (Clontech). Gene encoding mouse full-length GSDMD was ordered from Synobiological and tagBFP-encoding plasmid was from Evrogen. I105N point mutation was introduced by site-directed mutagenesis. tagBFP-tagged GSDMD variants and Dmrb-caspase-1 construct were prepared by overlap PCR using Phusion HF polymerase (Thermo Fisher Scientific). All mouse GSDMD gene variants were restriction digested by BamHI and EcoRI restriction nucleases and inserted into pRETROX Tre3G at BamHI/EcoRI sites.

Dimerizable caspase-1 construct Dmrb-caspase-1 (DMRB-DMRB-casp1ΔCARD) was digested by NotI and XbaI restriction nucleases and inserted into pcDNA3. I104N and L290D point mutations were introduced by site directed mutagenesis in ORFs encoding human NT and full-length GSDMD in pcDNA3.1, respectively.

For CRISPR/Cas9 targeting parental empty vectors pXPR-054-Blast or pXPR-053-Vex were digested with BsmbI restriction enzyme and the cut vector was purified by gel extraction. sgRNA-corresponding DNA oligos were ordered from IDT and designed based on the targeting sequence of guides found in the Brie library. Forward oligo sequences had the sequence CACCG added 5′ to the sgRNA targeting sequence. Reverse complement oligo sequences had the sequence AAAC added to the 5′ end and C added to the 3′ end. Equal molar quantities of forward and reverse oligos were allowed to anneal to each other and were phosphorylated for efficient ligation to the purified and digested parental vectors.

Primary BMDM generation and immortalization

Bone marrow derived macrophages (BMDMs) were differentiated from whole bone marrow derived from flushed tibia and femurs from C57BL/6J wild-type, NLRP3-deficient, gasdermin D-deficient, LysM CRE-expressing, LysM CRE x flox/flox Raptor, LysM CRE x flox/flox Rictor, and Cas9 knock in mice. BMDMs were also differentiated from CHIME reconstituted chimeras of WT control untargeted mice, RagA g1 targeted mice, and RagA g2 targeted mice. In brief, leg bones were surgically removed and cleaned of surrounding tissue. The bones were washed with sterile PBS and left in complete DMEM ((GIBCO) with 10% FBS (GIBCO) and Penicillin Streptomycin (GIBCO) with added supplements of L-glutamine (GIBCO) and sodium pyruvate (GIBCO) during extraction). The ends of tibia and femur were cut, and the bones were flushed with sterile PBS in a 10 mL syringe per bone and bone marrow from each individual mouse was pooled and pelleted at 400 x g for 5 minutes. ~10E6 bone marrow cells were used per non-TC coated 10 cm plate for differentiation. Differentiation was carried out in complete DMEM supplemented with 30% L929 supernatants containing M-CSF. J2 retrovirus secreting cells were passaged in complete DMEM and split every 2-3 days to prevent acidification and confluency. For immortalization viral supernatant production, flasks of J2 secreting cells were allowed to reach confluency and left to accumulate virus in their supernatants for 24 hours after reaching 100% confluency. Viral supernatants were spun at 400 x g to remove cell debris and passed through a 0.45 μm syringe filter to ensure no cellular cross-contamination. Two rounds of immortalization viral supernatants were placed on differentiating macrophage cultures and supplemented with 30% L929 supernatants. Transduced cells were allowed to recover in fresh complete DMEM with 30% L929 supernatants then split 1:2 or 1:3 as immortalized macrophages began to form clusters / colonies in non-TC coated 10 cm plates. Cells were progressively starved of M-CSF by reducing the L929 supernatant supplementation concentration over approximately 1.5-2 months until cells were able to grow without M-CSF and be split 1:10 every 2-3 days. Immortalized bone marrow derived macrophages (iBMDMs) were cultured in complete DMEM without L929 supernatant supplementation. Cells were washed in PBS pH 7.4 containing 2.5 mM EDTA to detach cells for passage. Cells were passaged 1:10 every 2-3 days to prevent overcrowding and media acidification.

Retroviral/Lentiviral transduction

For generating stable expression of Tet3G in Cas9 KI iBMDMs, pantrophic retrovirus particles were produced by transfecting plasmids pCMV-VSV-G (1.5 μg) and pRETROX Tet3G (2.5 μg) (Clontech) in Platinum-GP (Cell Biolabs) packaging cell line with Lipofectamine 2000 (10 μL). 3 days after transduction media was swapped for complete DMEM with 1.5 mg/ml G-418 for selection of productively transduced cells. For generating doxycycline inducible GSDMD variants in Cas9 KI Tet3G stable cells, amphotrophic retrovirus particles were produced by transfecting the respective pRETROX Tre3G plasmid (4 μg) into Gryphon Ampho (Alelle Biotechnology) packaging cell line with Lipofectamine 2000 (10 μL). Media was swapped for complete DMEM with 10 μg/ml puromycin and 1.5 mg/ml G-418 3 days after transduction. These cells were further single cell cloned by limiting serial dilution to yield clonal populations for purposes of magnitude and synchronization of doxycycline induction responses.

For generating CRISPR/Cas9 targeted cell lines, lentivirus particles produced by transfecting plasmids psPAX2, pMD2.G, and the transfer plasmid pXPR-054-Blast containing the sgRNA sequence of interest. We targeted RagA with two independent guide RNA sequences derived from the Brie library (g1: GGTTCCCCAAGAATCGGACG and g2: GATCAGCTGATAGACGATGC). We targeted RagC with two independent guide RNA sequences derived from the Brie library (g1: CTTCCAGGACGACTACATGG and g2: TTTCTGTACCACCTTACTGA). Plasmids were transfected into HEK293T cells in 10 cm dishes at a confluency of 50%–70% with Lipofectamine 2000 at a DNA to Lipofectamine ratio of 1:3. Media was changed 8-12 hours post DNA transfection and viral supernatants were collected 24 hours post media change. Viral supernatants were spun at 400 x g to remove cellular debris then passed through a 0.45 μm PVDF filter via syringe. Viral supernatants were placed directly on growing Cas9 expressing iBMDMs and spinfected at 1250

x g for 45 minutes at 30°C. These cell lines were selected with 10 μg/ml of Blasticidin to select for cells expressing sgRNA stably after transduction.

Chimeric immune editing

For generating CRISPR/Cas9 edited bone marrow chimeras for ablation of genes of interest in primary immune cells, we adapted a protocol known as CHimeric IMmune Editing (CHIME) as previously described (LaFleur et al., 2019). We targeted RagA with two independent guide RNA sequences derived from the Brie Library (g1: GGTTCCCCAAGAATCGGACG and g2: GATCAGCTGATA-GACGATGC). These correspond to the same guide RNA sequences used in the above pXPR-054-Blast vector for generation of RagA-deficient iBMDMs. We also utilized a control untargeted guide RNA sequence (GCGAGGTATTCGGCTCCGCG). These guide RNAs were cloned into a lentiviral expression vector pXPR-053, which expresses an sgRNA and the fluorophore Vex (a violet laser excited variant of GFP). Lentivirus was prepared by PEI-based transfection of HEK293x cells with Optimem containing pXPR-053 plasmids with described gRNAs and the packaging plasmids psPAX2 and pMD2.G. Lentivirus was isolated 72 hours post transfection, centrifuged at 2000 rpm for 5 minutes, and passed through a 0.45 μm filter to remove cells. The lentivirus was then concentrated by ultracentrifugation (20000 rpm, 2 hours, 4°C) using an SW28 rotor. Viral pellets were resuspended overnight in Ham's F12 media and frozen at −80°C. Viral titer was assessed on 293x cells. The mice used in these experiments were generated by crossing loxP-Stop-loxP-Cas9 mice (Jackson #026175) (Platt et al., 2014) to Zp3-Cre (Jackson #003651) to delete the Stop cassette in the germline and create a constitutive Cas9-expressing mouse strain. This resulting strain loxP-Cas9 was backcrossed greater than 10 generations to Jackson C57BL6/J mice (Jackson #000664). LSK bone marrow cells were isolated from femurs, tibias, and spines from Cas9-expressing mice. Briefly, bones were mechanically dissociated and LSK were enriched using a CD117 isolation kit (Miltenyi Biotec). Enriched bone marrow was stained with cKit (CD117), Sca-1, and lineage markers (Ter-119, CD3e, CD11b, Gr-1, B220, and CD5) and sorted on a BD Aria II for Lineage– Sca-1+ cKit+. LSK were plated overnight in PVA-containing media (500 mL Ham's F12 media with 10 mM HEPES, 1% ITSX, 1% Penicillin-Streptomycin, 1 mg/mL 87%–90% hydrolyzed polyvinyl alcohol, 10 ng/mL murine recombinant stem cell factor, and 100 ng/mL murine recombinant thrombopoietin). Non-TC coated plates were coated with retronectin overnight at 4°C. The next day, LSK were then spin transduced (1800 rpm for 90 minutes at 27°C) with lentiviral constructs on the retronectin-coated plates (MOI of 30). The transduced LSK cells were then cultured for one week in PVA-containing media splitting the cells every other day (Wilkinson et al., 2019). LSK were then sorted for Vex positivity and 50K cells per mouse were intravenously transferred into irradiated (2x 600 rad 3 hours apart) CD45.2 WT mice. These mice were administered Sulfamethoxazole-Trimethoprim in their drinking water for 2 weeks. After 8 weeks, Vex+ cells from the spleens and bone marrow of recipient mice were used for *in vitro* differentiation and *ex vivo* inflammasome assays.

For *ex vivo* splenocyte stimulations, spleens were surgically removed from deceased mice from WT control untargeted, RagA g1 targeted, and RagA g2 targeted bone marrow chimeras. Spleens were kept on ice in complete DMEM after removal. Whole spleens were homogenized using the plunger of a 10 mL syringe through a 70 μm cell strainer atop a 50 mL falcon tube. The cell strainer was washed with complete DMEM to collect residual single cells. Cells were pelleted at 400 x g for 5 minutes then subjected to ACK lysis buffer for 5 minutes. Cells were again pelleted and resuspended in complete DMEM and passed through a 40 μm cell strainer atop a 50 mL conical tube. Bulk splenocyte cells were counted, and 2E5 cells were dispensed into sterile FACS tubes for FlaTox stimulations. After stimulation, cells were stained with anti-CD11b antibody (Thermo, 1:200) and TruStain FcX (Biolegend) according to the manufacturer's protocol. These stained splenocytes were then analyzed on a Fortessa flow cytometer. Cells were analyzed for frequency of Vex+ (productive transduction of sgRNA construct) and CD11b high (splenic phagocyte). The ratio of Vex+, CD11b high splenocytes were compared from FlaTox-treated cells and single LFn-Fla component treated conditions to yield a ratio of depletion of splenic phagocytes after FlaTox treatment.

Brie cellular library and screening assay

Brie sgRNA only lentiviral library was obtained from the Broad Institute Genome Perturbation Platform. The Brie library contains expression constructs for sgRNA with coverage of 4 guides per gene in the murine genome and non-targeting controls. Our viral library coupled sgRNA expression to the expression of a blasticidin resistance gene for selection of productive transduction. Viral tittering prior to bulk library creation optimized transduction conditions. Increasing amounts of Brie library virus stock (0-500 μL) were added to 3E6 cells in prewarmed, complete DMEM with 5 μg/ml polybrene (in a constant final volume of 2 ml) in a 12-well plate. Spinfection transduction was performed by centrifugation at 1250 x g for 45 minutes at 30°C. After spinfection, 2 mL of complete DMEM was added and cells were incubated until the next day. Each condition was re-plated at lower density (1E5 cells/well of 6-well plate) in two wells to allow for ample room to grow during expansion and selection. In half of the wells, cells were selected with 4 μg/ml blasticidin for 4 days. At the end of selection and expansion, cell viability was measured to determine infection efficiency through a ratio of the number of blasticidin-resistant cells and the number of non-selected cells for each condition. The target efficiency is 30%–50% transduction efficiency by this assay to yield primarily 0.5-1 virus per productively transduced cell to ensure our downstream enrichment analysis could correlate guide abundance to a single perturbation (Doench et al., 2016).

Downstream screening assays should have 400 cells per single guide perturbation representation for statistical robustness during enrichment analysis (Doench et al., 2016). For our library creation, we utilized 9450 μL of stock virus on 189E6 engineered macrophages. After spinfection as described above, 2 mL of fresh complete DMEM was added to each well and cells were incubated for one day. 24 hours after spinfection, cells were detached with cold sterile PBS with 2.5 mM EDTA and replated into 175 cm^2

TC filter flasks (12E6 starting cells / flask). After one more day, selection was initiated using 4 μg/ml of blasticidin in complete DMEM that also contained 10 μg/ml puromycin and 1.5 mg/ml G418 to ensure our synthetic pathway was still maintained and productively transduced cells expressing sgRNA would also be selected and expanded. After 6 additional days, surviving cells were pooled and plated into 10 cm TC-coated dishes. ∼150E6 cells were induced with doxycycline to express the toxic NT-GSDMD molecule for 16 hours. Cells were detached with cold PBS with 2.5 mM EDTA and sequentially washed with MACS buffer (1%–2% FBS, 2.5 mM EDTA in pH 7.4 sterile PBS) to get rid of cellular debris and focus sorting analysis on intact and surviving cells. Cells were stained with PI solution (3.3 μg/ml) and sorted on an Aria cell sorter (BD). Cells were assayed for BFP fluorescence in the PacBlue channel and PI florescence in the PE-A channel. The top 15% BFP+, PI- cells were sorted as cells that may be defective for genes that promote GSDMD pore formation as they expressed the NT-GSDMD pore forming domain to high levels, but showed defective functional pore formation. Cells were sorted into PBS EDTA with 30% FBS to ensure efficient capture of cells/nuclei for downstream genomic DNA extraction. ∼200E6 cells were collected that were left uninduced to serve as an input control to account for potential skewing of guide abundance in our population during the expansion and screening assay (for example for guides targeting known tumor suppressors that may outgrow in the population). Genomic DNA was isolated using Nucleospin Blood XL (Clontech) according to Broad Genome Perturbation Platform protocols. The gDNA was also subjected to PCR inhibitor clean up columns from Zymo Research (D6030) then diluted to the desired concentration and number of wells and sent on dry ice to the Broad Institute for PCR amplification and next generation Illumina Sequencing. After PCR amplification of sgRNAs from genomic DNA, and subsequent next generation sequencing, the log-normalized sgRNA abundance from the input sample was subtracted from the log-normalized sgRNA abundance of BFP-positive survivors.

Doxycycline induction in engineered cell lines
Cell lines of different genotypes were counted using a Luna 2 cell counter and plated at 1E5 cells / well in a black 96 well plate with optically clear bottoms in 200 μL of complete DMEM. After cells adhered (> 6 hours resting in an incubator), media was replaced with warm complete DMEM or complete DMEM with doxycycline (0.5 μg/ml for initial characterization and 2 μg/ml for analysis of CRISPR/Cas9 edited clones). Cells were stained with diluted PI solution (final concentration 1:300) and lysis buffer or additional media were added to respective wells 30 minutes prior to a time point. The plate was spun at 400 x g for 5 minutes to ensure all cells were at the bottom of the well prior to adding the plate to the plate reader. Population PI staining was assayed with a Tecan plate reader or Biotek Synergy Mx. The program settings for PI inclusion assay were bottom reading of fluorescence with an excitation wavelength of 530 nm and emission wavelength of 617 nm. Supernatants from the spun down plate were taken for CyQuant LDH colormetric enzyme assay (Thermo) per the manufacturer's instructions. Cells were lifted directly with MACS buffer (1%–2% FBS, 2.5 mM EDTA in sterile pH 7.4 PBS) and assayed for frequency of PI+ cells and frequency of BFP+ cells on a Fortessa flow cytometer (BD). Associated flow cytometry data was analyzed using FlowJo 10.0. For live cell microscopy, diluted PI (final concentration 1:300) was added to the wells right after doxycycline addition. The plate was allowed to equilibrate with PI for 30 minutes prior to imaging to allow for setting of exposure, gain, and focus settings based on lysed wells. The plate was placed in the Biotek Cytation with 5% CO_2 and 37°C incubation with bright field and red channel images taken every 30 minutes for 8 hours.

Compound treatment
1E5 cells per well were seeded into 96 well black plates. Inhibitors/activators of mTOR pathway were added to cells at the same time as doxycycline (0.5 μg/ml). For inhibitors 14 hours endpoint PI and LDH measurement was selected. For activator MHY1486 early time point of 6 hours was selected to determine PI uptake and LDH release. Response of inhibitor-treated cells was normalized to untreated (0%) and uninhibited, Dox-treated samples (100%).

Neon electroporation
Electroporation was conducted using the Neon transfection machine, pipette, tips, and associated commercial buffers (Thermo-Fisher Scientific). For experiments involving electroporation of LPS into cells, 1.2E6 cells were suspended in 120 μL of R buffer from the Neon transfection kit. Either 1.2 μL of PBS or with 1.2 μL of 1 mg/ml LPS (effective dose of 1 μg of LPS per 1E6 cells in a 100 μL Neon pipette tip) were added to the cell suspension prior to electroporation. Cells were drawn into the Neon transfection pipette and electroporated with the parameters of Voltage 1400, pulse width 10 ms, and pulse number 2. For protein isolation, 1E6 cells were dispensed into 500 μL of L-glutamine and sodium pyruvate supplemented, serum-free OptiMEM to allow for analysis of whole lysate and supernatant combined through direct lysis with 5X SDS Laemmli buffer and TCEP reducing agent. For PI incorporation, LDH release, and supernatant collection for ELISA analysis of cytokines, the 100 μL containing 1E6 electroporated cells were dispensed into 900 μL of complete DMEM lacking antibiotics and 100 μL of this cell solution was dispensed into 6 wells for each condition in a black 96 well plate with optically clear plastic bottom. Of these wells, 3 wells served as internal lysis controls and 3 wells served as experimental conditions. Diluted PI solution (final concentration 1:300) was added to every well 30 minutes prior to the end time point. Lysis buffer or complete DMEM with no antibiotics were added to corresponding wells for PI and LDH normalization. Population PI staining was measured with a Tecan plate reader. For live cell microscopy, diluted PI (final concentration 1:300) was added to the wells right after plating. The plate was allowed to equilibrate with PI for 30 minutes prior to imaging to allow for setting of exposure, gain, and focus settings based on lysed wells. The plate was placed in the Biotek Cytation with 5% CO_2 and 37°C incubation with bright field and red channel images taken every 10 minutes for 1 hour.

To generate NINJ1 knock out macrophages via electroporation, 1E6 Cas9-expressing iBMDMs were electroporated with 2 μl of sgRNAs (sgRNA1: TGCCAACAAGAAGAGCGCTG; sgRNA2: GACCACAAGGGGCACGAAGA; pre-designed and ordered from IDT, diluted to 100 μM in nuclease-free H₂O) using the Neon transfection system (electroporation conditions as described above for LPS electroporations, Voltage 1400, pulse width 10 ms, and pulse number 2). After 3 days, gDNA was extracted from 1E5 cells using 50 μl of QuickExtract DNA extraction solution (Lucigen) according to manufacturer's protocol. The genomic region around exon 2 of NINJ1 was amplified by PCR (Fwd: TGTGTGCAGAGGTTGGTGTT; Rev: AGTCACAGCTTGGGCCATAC), and the resulting PCR product was sequenced by Sanger sequencing using the Fwd PCR primer. Sequencing traces from WT, guide 1 targeted, and guide 2 targeted cells were uploaded into ICE software tool by Synthego (https://ice.synthego.com/#/) to evaluate knock out efficiency, which was determined to be > 70% for both sgRNAs used.

Characterization of apoptosis
The PacBlue Annexin-V and 7-AAD apoptosis detection kit from Biolegend was used to characterize the apoptotic ability of LysM-CRE WT, Rictor-deficient, and Raptor-deficient iBMDMs in response to 1 μM of Staurosporine (STS) for 8 hours. The manufacturer's staining protocol was followed. Cells were analyzed by a Fortessa flow cytometer (BD). Double-positive (Annexin-V+, 7-AAD+) cells were quantified by quartile gating comparing unstimulated control cells and STS stimulated experimental conditions using FlowJo.

Bacterial infection
Salmonella enterica serovar Typhimurium (SL1344) was streaked on Luria Broth (LB) agar plates with no antibiotic selection to yield single colonies. Single colonies were picked with a sterile tip and used to inoculate a liquid culture of normal LB in 2.5 mL of a 14 mL bacterial culture tube and left to shake at 37°C for 12 hours. Cultures were back-diluted 1:20 into 2.5 mL of high salt LB (LB + 0.3M NaCl) to encourage an invasive phenotype for 3 hours shaking at 37°C. Liquid culture was analyzed undiluted and 1:10 diluted in high salt LB compared to a blank of high salt LB alone to measure an accurate OD600. It was assumed that an OD600 corresponded to roughly 1E9 bacteria / ml for purposes of MOI calculations. 1 mL of liquid culture was spun at 10,000 x g in a microcentrifuge tube for 5 minutes at 4°C to pellet bacteria. This pellet was sequentially washed in sterile PBS pH 7.4 for 3 washes and spins. Calculated amounts of bacteria to yield an MOI of 10 were added to either L-glutamine / sodium pyruvate supplemented antibiotic free Opti-MEM for protein isolation experiments or complete DMEM lacking antibiotics for plate reader experiments in a black 96 well plate with optically clear bottoms. Bacteria were spun down onto cells at 400 x g for 5 minutes to synchronize bacterial uptake by macrophage lines. 5X SDS laemmli buffer with TCEP reducing agent was added directly to protein isolation wells to yield a cellular lysate and low serum supernatant protein sample for western blot analysis. 30 minutes prior to end point, dilute PI solution (final concentration 1:300) was added to all wells in the 96 well plate. Lysis buffer or complete DMEM with no antibiotics were added to respective wells for PI and LDH normalization. At the end point time point of 1 hour, the plate was spun at 400 x g for 5 minutes to ensure all cells were at the bottom of the wells and PI fluorescence was read with a Tecan plate reader. Samples of supernatant were taken for LDH colorimetric enzyme assay.

Confocal microscopy
To follow localization of tagBFP-tagged gasdermin variants cells were seeded into μ-slide (Ibidi). Cells were non-treated or treated with doxycycline (0.5 μg/ml) for the defined time. 30 minutes prior the end of incubation period PI (3.33 μg/ml) was added. Cholera toxin subunit B-Alexa Fluor 647 (2 μg/ml) was added as well in the experiment to follow plasma membrane localization. Cells were observed under a Leica TCS SP5 laser scanning microscope mounted on a Leica DMI 6000 CS inverted microscope (Leica Microsystems, Germany) with an HCX plan apo 63X (NA 1.4) oil immersion objective used for imaging. A 405 nm laser line of 20 mW diode laser was used for tagBFP excitation, a 543 nm laser was used to follow propidium iodide, and a 633 nm laser was used for Cholera toxin subunit B-Alexa Fluor 647 excitation. To observe mitochondria, cells were followed at different time points after addition of doxycycline (0.5 μg/ml), Mitotracker Deep Red FM (30 nM) and PI (3.33 μg/ml).

Detection of cellular ROS
A day before stimulation, 3E5 cells were seeded per well of 24-well plate. For detection of intracellular ROS, CellRox Deep Red reagent (final concentration of 5 μM) was added to cells 7.5 hours after doxycycline stimulation. After 30 mins incubation in CO₂-incubator, cells were washed with PBS and detached with PBS/EDTA. Samples were analyzed by flow cytometry using Cytek Aurora and FlowJo. Mean fluorescence intensity of morphologically intact population was analyzed.

Mitochondrial ROS and mitochondrial potential
For detection of mitochondrial ROS, cells were detached after 8 h-stimulation with doxycycline and incubated with MitoSOX (5 μM) for 20 minutes at 37°C in PBS/2% FBS. After washing step, samples were followed by flow cytometry using Cytek Aurora and analyzed using FlowJo. Fraction of MitoSOX-positive cells from morphologically intact population was analyzed.

Detection of change in mitochondrial potential was followed with TMRM (tetramethylrhodamine, methyl ester, perchlorate). Cells in 96 well black microtiter plates were stimulated with doxycycline (0.5 μg/ml) for 7 hours after which TMRM (final concentration 100 nM) was added for one hour. Medium was replaced with PBS/2% FBS and TMRM fluorescence was measured with Synergy Mx (Biotek) with 535 nm excitation and 600 nm emission settings. TMRM fluorescence was normalized to untreated control as 100%. To follow TMRM fluorescence using flow cytometry, cells were detached after 7.5 hour stimulation with doxycycline and incubated with TMRM

(100 nM) for 30 minutes at 37°C in PBS/2% FBS. After washing step, samples were followed by flow cytometry using Cytek Aurora and analyzed using FlowJo. Mean fluorescence intensity of morphologically intact population was analyzed. MFI of samples 8 hours after doxycycline addition was normalized to non-treated (100%) and unlabeled (0%) control.

Activation assays in HEK293T and HEK293 cells

To follow human GSDMD variants' constitutive pore-forming activity and Myd88 L265P stimulation of NF-κB activation, control HEK293T (WT) and RagA/B-DKO HEK293T cells (a kind gift from D.M. Sabatini (Rogala et al., 2019)) were seeded (25-55 E4/well) into black or white 96 well plate (Corning). The next day, cells were transfected with plasmids containing human GSDMD variants using Lipofectamine 2000. 20 hours later cells were analyzed for PI uptake and LDH release using Synergy Mx microtiter plate reader (Biotek). To determine % of PI uptake and LDH release, results were normalized to control plasmid transfected cells (0%) and lysed cells (100%). To follow Myd88 L265P activity, cells were transfected with pcDNA3 Myd88 L265P or empty vector, pELAM1-F-luciferase, phRL-TK Renilla luciferase (R-luc) plasmid mixture with Lipofectamine 2000. The total DNA in transfection mixture was kept constant in all conditions. Cells were lysed 24 hours later in Passive lysis buffer (Promega). Luciferase activity was followed upon coelentrazine and luciferin addition on Orion microtiter plate reader. Relative luminescence units were determined as ratio between F-luciferase and R-luciferase activity and normalized to control response (empty vector (pcDNA3) transfected cells).

4E4 HEK293 cells were seeded per well of 96 well black or white microtiter plate. The next day, cells were transfected with plasmid encoding Nt I104N hGSDMD (30 ng) and different amounts of plasmid encoding TSC-1 (170 ng, 100 ng, 0 ng). 20 hours later cells were analyzed for PI uptake and LDH release using Synergy Mx microtiter plate reader (Biotek). To follow Myd88 L265P activity, cells were transfected with Myd88 L265P or empty vector and pELAM1-F-luciferase/phRL-TK Renilla luciferase plasmid mixture and different amounts of plasmid encoding TSC-1 (140 ng, 100 ng, 0 ng). The total DNA in transfection mixture was kept constant in all conditions. Fold RLUs were calculated by normalizing Myd88 L265P response to empty vector control.

Starvation experiment

Dialyzed FBS was prepared by dialysis against PBS using 3500 MWCO dialysis tubes. 10X amino acid (AA) solution was prepared by mixing essential and nonessential AA solutions and L-glutamine and adjusting pH to 7.2.

3.5E4 HEK293T cells were seeded per well of black microtiter well plate. The next day cells were transfected with 70 ng of Dmrb-caspase-1 plasmid, 10 ng of full-length human GSDMD plasmid and 20 ng of pcDNA3 and 0.5 μL of Lipofectamine 2000. For western blot analysis experiment was performed in 24-well plate format. The number of cells and amount of transfection mixture was adjusted accordingly. The next day, cells were washed with DMEM without amino acids and glucose. After wash, medium containing dialyzed FBS and glucose was added, and cells were incubated for 50 minutes. 10X amino acid solution or DMEM without AA was added to final concentration of 1X. Homodimerizing molecule A20187 was added at the same time (final concentration 500 nM). LDH release was measured 4 hours later. To determine % of PI uptake and LDH release, results were normalized to control plasmid transfected cells (0%) and lysed cells (100%).

Subcellular fractionation

WT, RagA KO, and RagC KO iBMDMs (10E6 cells) were seeded in 15 cm tissue culture plates and incubated overnight at 37°C and 5% CO_2. On the next day, transgene expression was induced by culturing cells in complete DMEM containing 2 μg/ml of doxycycline for 8 hours. Cells were lifted with PBS with 2.5 mM EDTA and washed once with 1 mL of hypotonic buffer (10 mM Tris pH 7.4, 1.5 mM $MgCl_2$, 10 mM KCl, complete mini protease inhibitors). Cells were centrifuged (400 x g for 3 min at 4°C) and pellet was resuspended in 750 μl hypotonic buffer followed by incubation on ice for 30 min. Swelled cells were then homogenized by passing them 50 times through a 26-gauge needle. Nuclei and cell debris were pelleted by centrifugation at 2,500 x g for 5 min at 4°C. A small fraction of the post-nuclear supernatant was removed and used as an input control for western blotting. Supernatants were transferred to a new set of tubes and centrifuged again at 17,000 x g for 30 min at 4°C to pellet cellular membranes. The supernatant (cytosolic fraction) was removed, and membrane pellet was washed three times with 1 mL of hypotonic buffer. Samples for immunoblotting were prepared by adding an appropriate amount of 5X SDS loading buffer + 10X TCEP to cytosolic fraction and resuspending membrane pellet in an equal amount of 1X SDS loading buffer + TCEP. These protein samples were heated to 65°C for 10 min. Presence of NT-GSDMD-BFP fusion protein in each fraction was determined by western blot using a rabbit anti-tagBFP primary antibody. Tubulin (mouse primary antibody from DSHB, 1:100 dilution) and Na^+/K^+ ATPase (rabbit primary antibody from CST, diluted 1:1000) served as control markers for the cytosol and membrane fraction, respectively.

GSDMD oligomerization assay

WT, RagA KO, and RagC KO iBMDMs (1E6 cells per condition in 2 mL of complete DMEM) were seeded in 12-well plates and incubated at 37°C and 5% CO_2 for 1 hour to allow cells to attach. Media was exchanged for 1 mL of Opti-MEM containing 2 μg/ml of doxycycline to induce the expression of NT-GSDMD-BFP for 8 hours at 37°C and 5% CO_2. As indicated, 50 μl of Opti-MEM containing mitochondrial poisons (10 μM rotenone, 10 μg/ml antimycine A, 100 μM TTFA final diluted concentration) or H_2O_2 (625 μM, 1.25 mM, or 3.125 mM final diluted concentrations) were added to cell culture media after 4 hours to induce ROS. 250 μL of 5X SDS loading buffer was added directly to each well to capture proteins present in both the cell lysates and cell culture supernatants. Samples were split equally into two tubes and 75 μL of TCEP or dH_2O was added to generate

non-reducing and reducing western blot samples. After heating to 65°C for 10 min, proteins were separated by SDS-PAGE on a 4%–12% acrylamide gradient gel (ThermoFisher Scientific) and NT-GSDMD-BFP transgene was detected by western blot. The assembled GSDMD pore is resistant to SDS under non-reducing conditions, thus oligomerization of NT-GSDMD-BFP was indicated by a gel shift toward higher molecular weight.

FRAP of CD14 and NT-GSDMD-BFP

Fluorescence recovery after photobleaching (FRAP) experiments were performed on a Zeiss 880 laser scanning confocal microscope using the in-built FRAP module within the microscope control software Zen Black. Empty vector WT Dox-inducible NT-GSDMD-BFP or RagA KO and RagC KO cells were plated on the 35 mm μ-Dish (Ibidi; Munich, Germany) and stained with PE conjugated anti-CD14 antibody (1:200) for 20 minutes at 37°C. Staining media was aspirated, and cells were washed twice with warm complete DMEM. After 8 hours of doxycycline induction of NT-GSDMD-BFP, endogenous BFP was also subjected to FRAP analysis in these genotypes. Cells were scanned using a 63X oil immersion lens with the 405 nm laser. Regions of interest (ROI) were created at cell membranes and fluorescence bleached by rapid scanning of increased laser power (5%–10%) to a bleach depth of 40%–60%. Time-lapse images were acquired over a 3-minute time course post-bleaching at 2 s intervals. Images were processed in Zen and FRAP data were fit to a single exponential model using GraphPad Prism.

Data analysis was performed using previously published methods (Haggie and Verkman, 2008). Fluorescence intensities of ROI in the bleaching area (ROIb = bleached area) were recorded for each time point. The final data was normalized to pre-bleached intensities of the ROIs data and fitted to a single exponential recovery curve. Percent fluorescence recovery (mobile fraction) was calculated from the plateau (Vmax) of the fitted curves normalized to the total bleached fluorescence.

Purification of LFn-Fla from insect cells

We adapted the protocol detailed from (Rauch et al., 2017; Rauch et al., 2016) to produce LFn-Fla in insect cells using the Bac-to-Bac baculoviral expression system (ThermoFisher Scientific). In brief, Sf9 cells were initially seeded at a density of 1E6 cells/ml in 750 mL of Hyclone SFX-insect media (GE Life Sciences) and grown overnight at 27°C at 110 rpm. 10 mL of P2 or P3 virus for expression of LFn-Fla was added with an additional 250 mL of media and grown at 27°C at 110 rpm for 72 hours. The insect cell pellets were collected by first spinning in large buckets at 1000 x g for 20-30 minutes. The cells were resuspended in PBS and transfered into a 50 mL conical tube (rated for high-speed centrifugations). All following steps were performed at 4°C and / or on ice. The 50 mL conical tube of cells was centrifuged at 1000 x g for 10 minutes. We resuspended the insect cell pellet in 50 mL of lysis buffer (25 mM HEPES-NaOH pH 7.4, 150 mM NaCl, 10 mM Imidazole) supplemented with complete protease inhibitor tablets and split into two 50 mL falcon tubes. We lysed these 25 mL fractions via sonication. An additional 25 mL of lysis buffer + 1 mM PMSF + 2 mM Benzamidine were added to each tube. The tubes were centrifuged at 20,000 x g for 45 minutes at 4°C to clarify the lysate. We equilibrated 1 mL of Ni-NTA agarose beads in lysis buffer (corresponds to 2 mL of a 50% ethanol slurry). Beads were added to the clarified lysate and incubated at 4°C for 1 hour while rotating. We washed the beads with a total of 50 mL of lysis buffer and combined into one tube. After a subsequent spin, we resuspended the beads in 25 mL of lysis buffer and poured into a gravity flow column (BioRad polyprep column). We washed the beads on the column with one column volume (∼25 ml) of wash buffer (pH 7.4 25 mM HEPES-NaOH, 400 mM NaCl, 25 mM Imidazole).

Elution was performed with 5X the bead volume (∼5 ml) of elution buffer (pH 7.4 25 mM HEPES-NaOH, 150 mM NaCl, 250 mM Imidazole). Buffer was exchanged into ion exchange chromatorgraphy (IEX) buffer A (25 mM Tris-HCl, pH 7.5) with PD-10 Desalting columns (GE Healthcare). IEX was performed on BioRad FPLC system (using HiTrap Q HP 1 mL column and loaded with a 10 mL loop) with a gradient from 0%–100% of IEX buffer B (25 mM Tris-HCl pH 7.5, 1 M NaCl). The protein of interest was eluted as one single peak. Presence of protein of interest in peak fractions was confirmed by SDS-PAGE followed by InstantBlue staining (Expedeon). Protein concentration in pooled peak fractions was determined by measuring absorbance at 280 nm on a nanodrop device. 10% glycerol was added to pure protein and snap-frozen aliquots were stored at −80°C.

FlaTox stimulation in unprimed phagocytes

LFn-Fla was purified from insect cultures as described above. Aliquots of LFn-Fla were snap-frozen at a concentration of 0.5 mg/ml. Protective antigen (PA) was bought from a commercial vendor (List Biological Laboratories) and resuspended in sterile PBS pH 7.4 containing 10% glycerol to a concentration of 1 mg/ml and snap-frozen. For all stimulations, LFn-Fla and PA were diluted to a 2X working concentration in complete DMEM. To create 1X PA only treatments an equal volume of complete DMEM and 2X PA were combined. To create 1X LFn-Fla only treatments an equal volume of complete DMEM and 2X LFn-Fla were combined. To create 1X FlaTox treatments an equal volume of 2X PA and 2X LFn-Fla were combined. For iBMDM and BMDM stimulations, a final concentration of 250 ng/ml of PA and 100 ng/ml of LFn-Fla were used. For splenocyte stimulation, a final concentration of 250 ng/ml of PA and 500 ng/ml of LFn-Fla were used. For NAC experiments with iBMDM, NAC (Sigma) was reconstituted in sterile PBS pH 7.4 and pH was adjusted to pH 7.2-7.4 with NaOH. The final concentration of NAC stocks after pH adjustment was 200 mM. NAC stock solution was aliquoted into sterile tubes and kept at −20°C. For PI plate reader experiments, 1E5 cells were treated with 0 mM, 5 mM, or 15 mM NAC with respective stimulations in complete DMEM for 2 hours. For protein isolations, 1E6 cells were treated with 0 mM or 15 mM NAC with respective stimulations in supplemented Opti-MEM for 2 hours and directly lysed (supernatant and cells) with corresponding amounts of 5X SDS + 10X TCEP. Samples were heated for 10 minutes at 65°C, needled, then run on SDS-PAGE to investigate GSDMD cleavage by western blot.

Antibodies and reagents

LPS from *E. coli*, serotype 0111:B4 was supplied by Enzo (ALX-581-012-L002). Nigericin was purchased from Invivogen (tlrl-nig-5) or Sigma (N7143). Propidium iodide (PI) was purchased from Sigma (P4864-10ML). LDH activity was assayed using legacy Pierce LDH Cytotoxicity Assay Kit from ThermoFisher Scientific (88954) and replaced by CyQuant LDH Cytotoxicity Assay Kit from ThermoFisher Scientific according to the manufacturer's protocol (C7026). Mouse IL-1β release was quantitatively measured from cell-free culture supernatants using the Invitrogen IL-1β Mouse Uncoated ELISA Kit (88-7013-88) according to the manufacturer's protocol. For FACS analysis, the APC-conjugated antibody against CD11b from ThermoFisher Scientific (formerly eBioscience, 17-0112-82, 1:200) was used. For bone marrow FACS sorting, the APC-conjugated antibody against CD117 from Biolegend (135108, 1:100), the BV421-conjugated antibody against Sca-1 from Biolegend (108128, 1:100), the PE-conjugated antibody against Ter-119 from Biolegend (116208, 1:100), the PE-conjugated antibody against CD3ε from Biolegend (100308, 1:100), the PE-conjugated antibody against CD11b from Biolegend (101208, 1:100), the PE-conjugated antibody against Gr-1 from Biolegend (108408, 1:100), the PE-conjugated antibody against B220 from Biolegend (103208, 1:100), and the PE-conjugated antibody against CD5 from Biolegend (100608, 1:100) were used. For FRAP imaging analysis, the PE-conjugated antibody against CD14 from ThermoFisher Scientific (formerly eBioscience, 12-0141-82, 1:200) was used. For western blots, primary antibodies were used to detect proteins of interest including antibodies to tagBFP from Evrogen (AB233, 1:1000), Tet3G transactivator from Takara (631131, 1:1000), spCas9 from Cell Signaling Technologies (65832S, 1:1000) and from Abcam (ab191468, 1:1000), RagA from Cell Signaling Technologies (4357S, 1:1000), RagC from Cell Signaling Technologies (5466S, 1:1000), Raptor from Cell Signaling Technologies (2280S, 1:1000), Rictor from Cell Signaling Technologies (2114S, 1:1000), GSDMD from Abcam (ab209845, 1:1000), caspase-11 from Biolegend (647202, 1:500), human cleaved GSDMD from Abcam (ab210070, 1:1000), human GSDMD from Abcam (ab215203, 1:1000), phospho-p70 S6 kinase (Thr389) (1:1000) and p70 S6 kinase (49D7) (1:2000), Na^+/K^+ ATPase from Cell Signaling Technologies (3010S, 1:1000), and β actin from Sigma (A5441, 1:5000) and Cell Signaling Technologies (3700S and 4967, 1:5000), β tubulin from DHSB (clone E7, 1:100) and pro-IL-1β from GeneTex (GTX74034, 1:1000). Secondary antibodies to respective species with conjugated HRP were from Jackson ImmunoResearch or Abcam and used at 1:5000 (anti-mouse HRP 115-035-003, anti-rat HRP 112-035-003, anti-rabbit 111-035-003, anti-rabbit ab6721). Chemoluminescent signal substrate for HRP was SuperSignal West Pico (34577) and Femto Chemiluminescent Substrate (34095) from ThermoFisher Scientific and ECL from Amersham, GE Healthcare Life Sciences (RPN2232).

QUANTIFICATION AND STATISTICAL ANALYSIS

Analysis of screening results

Log-normalized sgRNA abundance was provided by the Broad GPP from input and BFP+/PI- survivor cells populations. Population bias during expansion and assay were corrected for by subtraction of input log-normalized sgRNA abundance from log-normalized sgRNA abundance from the BFP+/PI- survivor cell population. We used the Broad GPP web portal for further analysis: https://portals.broadinstitute.org/gpp/public/. A strict Chip file (CP1139 from Broad GPP) was used to map perturbations to sites in the genome, and the normalized data was subjected to hypergeometric analysis without replacement. In this method, the rank of sgRNAs is used to calculate gene p-values using the probability mass function of a hypergeometric distribution. P-values are generated by calculating the average $-\log_{10}$(p-value) in both directions and picking the more significant one. The top n% of sgRNAs per gene can be used to calculate the average p-value with this method. The average log-fold change per gene is also reported and this can be used to assess the magnitude of effect. Data displayed on the volcano plot requires a minimum of 3 out of 4 guides being present.

For gene ontology functional analysis of our screen results, the complete rank list based on most positive log-fold change (LFC) to most negative LFC was input into the GOrilla web tool: http://cbl-gorilla.cs.technion.ac.il/.

Microscopy image processing

For acquisition and image processing, Leica LAS AF software was used where threshold, brightness and contrast were adjusted. All images from the same experiment were processed in the same way using the same parameters. Mitotracker Deep Red FM fluorescence was calculated with particle analysis tool in ImageJ where also initial thresholding to reduce non-mitochondrial stain was performed. Cells from 3-5 246x246 μm^2 frames per experimental point were counted with CellCounter plugin in ImageJ. All images from the same experiment were processed in the same way using the same parameters. Composite figures were assembled in Microsoft Powerpoint.

Statistical analysis

Statistical significance for experiments with multiple groups and multiple independent variables were tested with two-way ANOVA with Tukey, Dunnett, or Sidak multiple comparison test corrections. One-way ANOVA with Dunnett multiple comparison test correction was used for analysis of multiple groups with a single independent variable. Unpaired two-tailed t test was used for comparison of two groups. Adjusted p-values were calculated with Prism 8.0 from GraphPad and the designation of * corresponds to $p \leq 0.05$, ** corresponds to $p \leq 0.01$, *** corresponds to $p \leq 0.001$, and **** corresponds to a $p \leq 0.0001$ in the figures. Data presented is representative of at least 3 independent experiments for western blots unless otherwise designated in figure legends. Data presented as quantified bar graphs or time course analysis is the combined means of 3 independent experiments unless otherwise designated in figure legends. Data with error bars are represented as mean ± SEM.

Supplemental figures
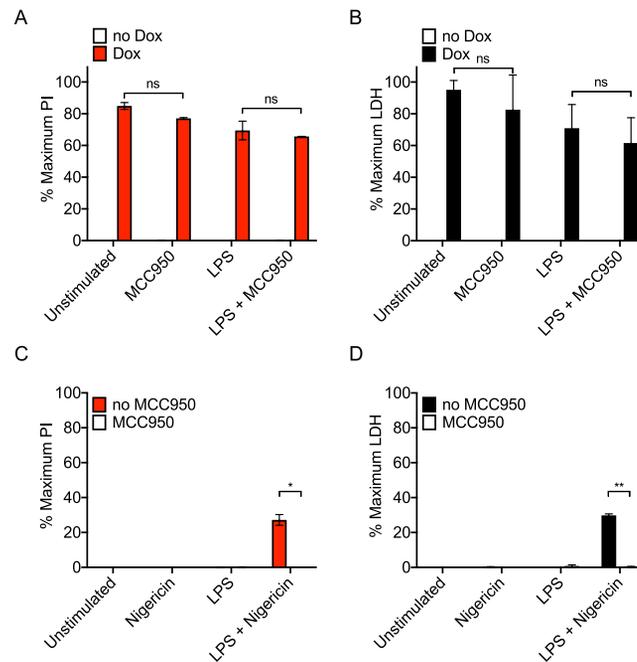
Figure S1. Inhibition of NLRP3 inflammasome does not affect pore formation and pyroptosis induced by NT-GSDMD, related to Figure 1

(A, B) PI uptake by plate reader to measure bulk membrane permeability (A) and LDH release into cell free supernatants to measure bulk cellular lysis (B) after Dox induction (0.5 μg/ml) of NT-GSDMD-BFP in iBMDMs with or without MCC950 pretreatment (5 μM for 30 minutes) for 13 hours. Cells were primed for 5 hours with LPS (100 ng/ml) prior to Dox addition.

(C, D) PI uptake (C) and LDH release into cell free supernatants (D) in LPS primed (100 ng/ml for 5 hours) and Nigericin stimulated (5 μM for 1 hour) WT iBMDMs with or without MCC950 pretreatment (5 μM for 30 minutes).

All quantifications represent the mean and SEM of two independent experiments. Unpaired two-tailed t test was used for analysis.

A

Dox   –   +   –   +   –   +

70 ——   α - p-S6K

70 ——   α - S6K

55 ——   α - β actin
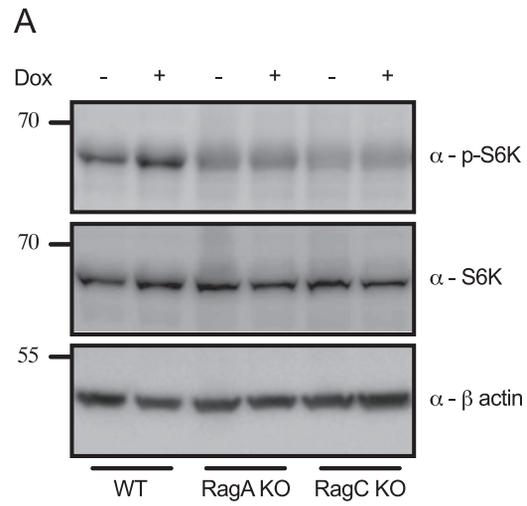
WT   RagA KO   RagC KO

Figure S2. mTORC1 activity is decreased in RagA-deficient and RagC-deficient cells, related to Figure 2

(A) western blot of phosphorylated S6K (Thr389) and total S6K with β actin loading control in WT, RagA KO, and RagC KO iBMDM lysates.
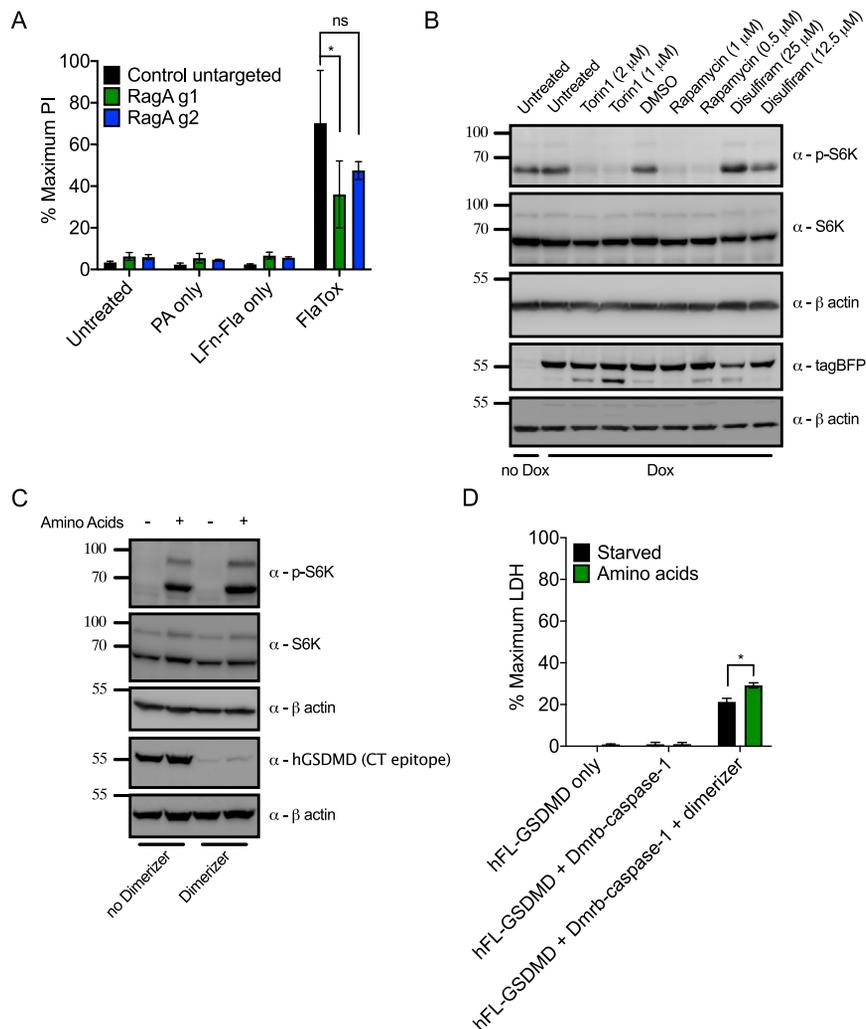
Figure S3. Amino acid stimulation of mTORC1 promotes NT-GSDMD mediated pyroptosis, related to Figure 3

(A) PI uptake analysis of WT and RagA targeted primary BMDMs after 2 hours of FlaTox treatment.

(B) western blot of the proteins indicated after Dox induction (0.5 μg/ml) and compound treatment for 7 hours.

(C) western blot of transfected 293T cells expressing a small molecule dimerizable caspase-1 (Dmrb-caspase-1) and hFL-GSDMD. Cells were starved of amino acids for 50 min then treated with amino acids and dimerizer compound. Phosphorylated S6K, total S6K, and hFL-GSDMD were assessed with corresponding β actin loading controls 4 hours after amino acid supplementation and addition of the dimerizer compound A20187. Note that two forms of S6K are detected, p85 and p70.

(D) LDH release into cell-free supernatants from cells transfected and treated as in (C).

Mean and SEM of three (A, D) independent experiments are shown. Two-way ANOVA with Tukey multiple comparison test (A) and unpaired two-tailed t test (D) were used for analysis.
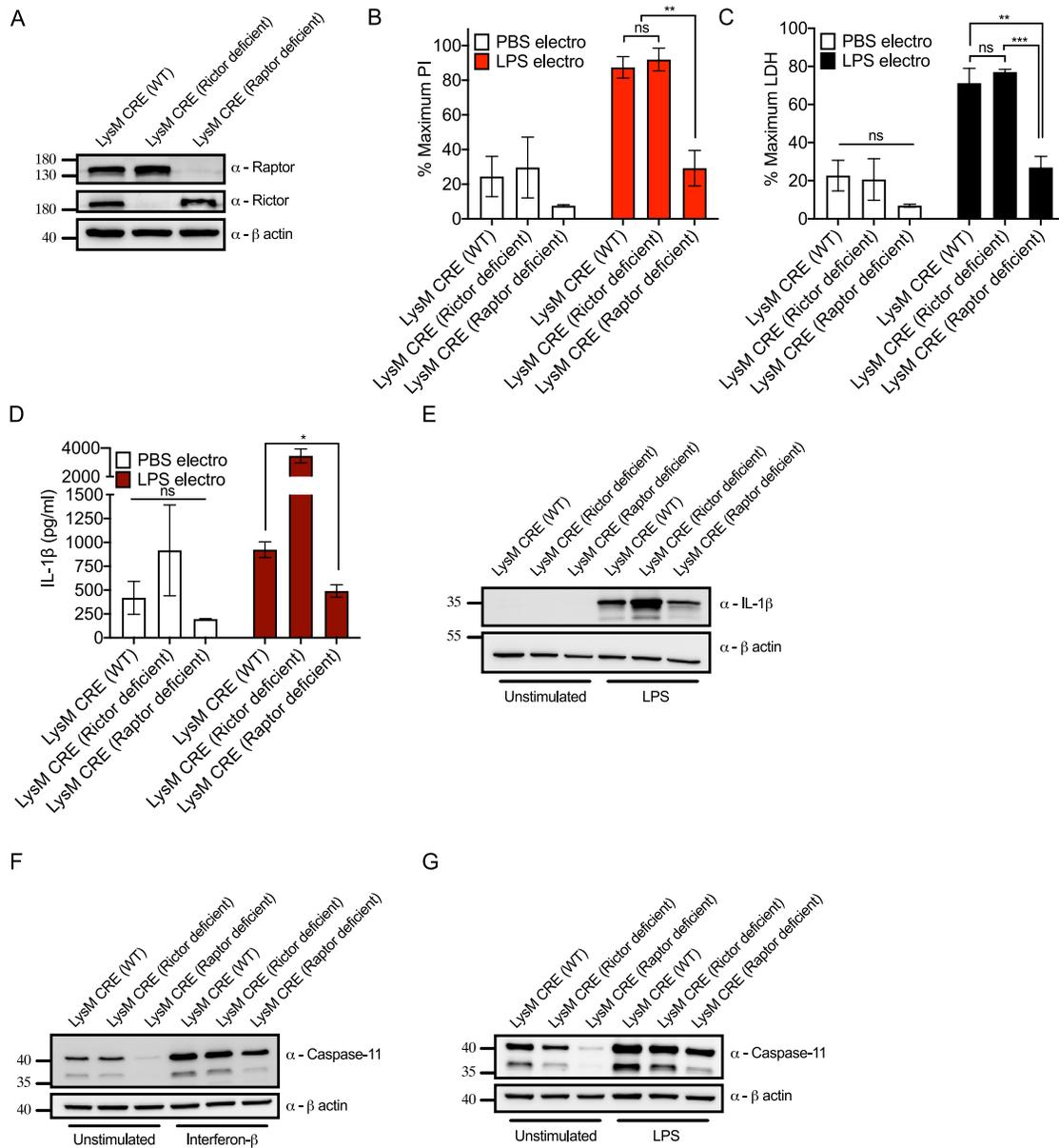
Figure S4. Analysis of LysM CRE, Rictor-deficient, and Raptor-deficient iBMDMs, related to Figure 4

(A) western blot of the proteins indicated from lysates of unstimulated iBMDMs of LysM CRE, Rictor deficient, and Raptor deficient cells.

(B, C) PI uptake analysis (B) and LDH release into cell-free supernatants (C) from LysM-CRE WT, Rictor-deficient, and Raptor-deficient iBMDMs primed with LPS (1 μg/ml) for 3 hours then electroporated with PBS or 1 μg of LPS. Electroporated cells plated for 3 hours before analysis.

(D) IL-1β ELISA measurements of cell-free culture supernatants from LysM-CRE WT, Rictor-deficient, and Raptor-deficient iBMDMs primed with LPS (1 μg/ml) for 3 hours then electroporated with PBS or 1 μg of LPS. Electroporated cells plated for 3 hours before analysis.

(E) western blot analysis of the proteins indicated from lysates of unstimulated or LPS (1 μg/ml for 3 hours) stimulated iBMDMs from LysM CRE, Rictor deficient, and Raptor deficient genotypes.

(F) western blot analysis of the proteins indicated from lysates of unstimulated or LPS (1 μg/ml for 3 hours) stimulated iBMDMs from LysM CRE, Rictor deficient, and Raptor deficient genotypes.

(G) western blot analysis of the proteins indicated from lysates of unstimulated or IFNβ (1000U for 3 hours) stimulated iBMDMs from LysM CRE, Rictor deficient, and Raptor deficient genotypes.

Mean and SEM of three independent experiments are shown. Two-way ANOVA was used for analysis.
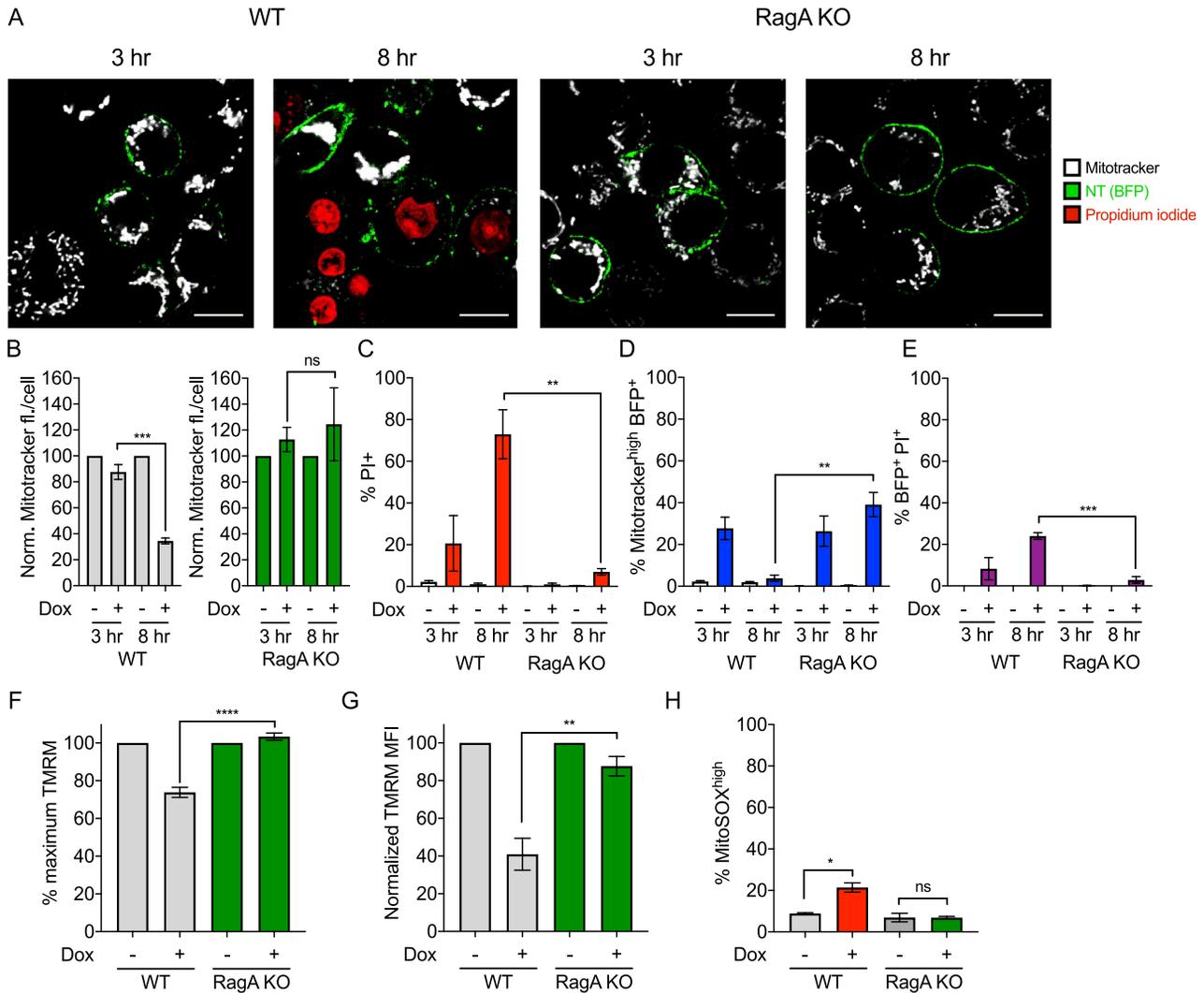
Figure S5. RagA-deficient cells are resistant to mitochondrial damage, related to Figure 6

(A) Live cell confocal microscopy of mitochondria labeled with Mitotracker Deep Red stain (white), nuclei of porous cells with PI (red) and NT-GSDMD expression (green) in WT and RagA KO cells. Images were taken at defined times after Dox addition. Scale bar indicates 10 μm.

(B-E) To quantify cells enriched in Mitotracker Deep red stain (B), PI+ cells (C), Mitotracker Deep Red highly fluorescent and BFP+ cells (D) as well as BFP+ and PI+ cells (E) 3-5 246x246 μm² frames were analyzed per experimental point. Mitotracker fluorescence was normalized to uninduced controls.

(F) TMRM fluorescence analysis by plate reader of WT and RagA KO iBMDMs after 8 hours of Dox induction (0.5 μg/ml). Values were normalized to uninduced controls.

(G) TMRM MFI in WT and RagA KO iBMDMs after 8 hours of Dox induction. MFI values were normalized to uninduced controls.

(H) Frequency of MitoSOX highly positive cells after 8 hours of Dox induction in WT and RagA KO cells. Mean and SEM of MitoSOX-enriched fraction of intact (live) cells is presented.

Mean and the SEM of three (B, C, D, E, G, H) or five (F) independent experiments are shown. Unpaired two-tailed t test (B, C, D, E, F, G) or two-way ANOVA (H) were used for analysis.
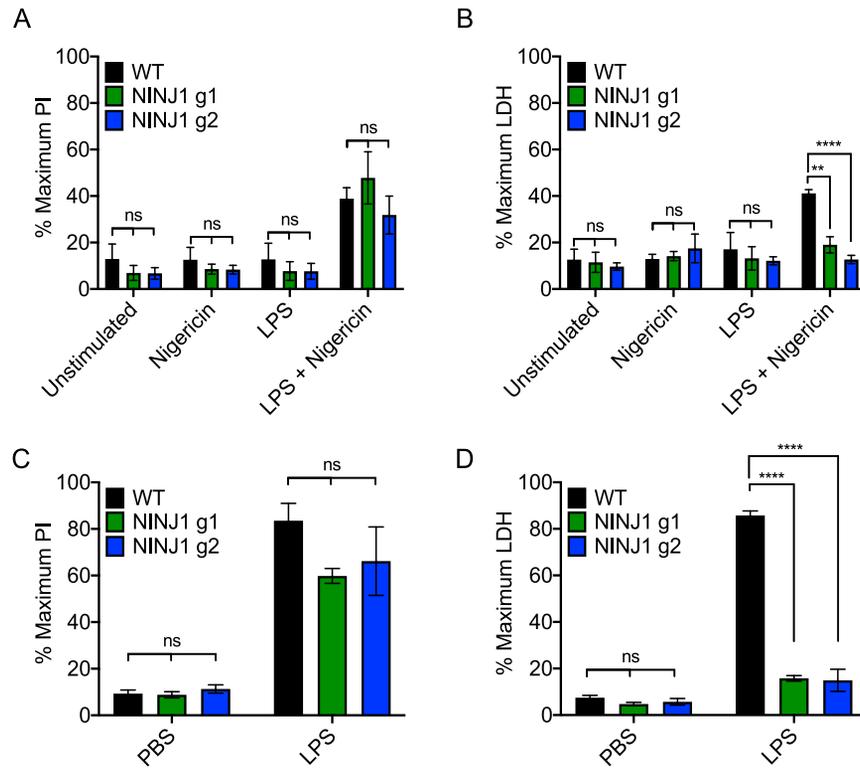
Figure S6. NINJ1 deficiency affects lysis but not GSDMD pore formation, related to Figure 6

(A, B) PI uptake analysis by plate reader (A) and LDH release into cell-free supernatants (B) was assessed from Cas9-WT, NINJ1 g1, and NINJ1 g2 iBMDMs primed with LPS (1 μg/ml) for 3 hours then treated with Nigericin (10 μM) for 2 hours.

(C, D) PI uptake analysis by plate reader (C) and LDH release into cell-free supernatants (D) was assessed from Cas9-WT, NINJ1 g1, and NINJ1 g2 iBMDMs primed with LPS (1 μg/ml) for 3 hours then electroporated with PBS or 1 μg of LPS. Electroporated cells were plated for 2 hours before analysis.

Mean and SEM of 3 independent experiments are shown. Two-way ANOVA was used for analysis.